Chapter 3

Molecular inventories and chemical evolution of low-mass protostellar envelopes

Abstract

This paper presents the first substantial study of the chemistry of the envelopes around a sample of 18 low-mass pre- and protostellar objects for which physical properties have previously been derived from radiative transfer modeling of their dust continuum emission. Single-dish line observations of 24 transitions of 9 molecular species (not counting isotopes) including HCO^+, N_2H^+, CS, SO, SO_2, HCN, HNC, HC_3N and CN are reported. The line intensities are used to constrain the molecular abundances by comparison to Monte Carlo radiative transfer modeling of the line strengths. In general the nitrogen-bearing species together with HCO^+ and CO cannot be fitted by a constant fractional abundance when the lowest excitation transitions are included, but require radial dependences of their chemistry since the intensity of the lowest excitation lines are systematically underestimated in such models. A scenario is suggested in which these species are depleted in a specific region of the envelope where the density is high enough that the freeze-out timescale is shorter than the dynamical timescale and the temperature low enough that the molecule is not evaporated from the icy grain mantles. This can be simulated by a "drop" abundance profile with standard (undepleted) abundances in the inner- and outermost regions and a drop in abundance in between where the molecule freezes out. An empirical chemical network is constructed on the basis of correlations between the abundances of various species. For example, it is seen that the HCO^+ and CO abundances are linearly correlated, both increasing with decreasing envelope mass. This is shown to be the case if the main formation route of HCO^+ is through reactions between CO and H_3^+, and if the CO abundance still is low enough that reactions between H_3^+ and N_2 are the main mechanism responsible for the removal of H_3^+. Species such as CS, SO and HCN show no trend with envelope mass. In particular no trend is seen between "evolutionary stage" of the objects and the abundances of the main sulfur- or nitrogen-containing species. Among the nitrogen-bearing species abundances of CN, HNC and HC_3N are found to be closely correlated, which can be understood from considerations of the chemical network. The CS/SO abundance ratio is found to correlate with the abundances of CN and HC_3N, which may reflect a dependence on the atomic carbon abundance. An anti-correlation is found between the deuteration of HCO^+ and HCN, reflecting different temperature dependences for gas-phase deuteration mechanisms. The abundances are compared to other protostellar environments. In particular it is found that the abundances in the cold outer envelope of the previously studied class 0 protostar IRAS 16293-2422 are in good agreement with the average abundances for the presented sample of class 0 objects.

Jørgensen, Schöier & van Dishoeck, 2004, A&A, 416, 603

3.1 Introduction

Understanding the chemistry of protostellar environments is important in order to build up a complete and consistent picture for the star-formation process. Detailed knowledge about the chemistry is required in order to fully understand the physical processes since it regulates the ionization balance and the gas temperature through cooling of the molecular gas, for example. At the same time the chemistry may potentially serve as a valuable tool, both as a time indicator for the protostellar evolution and as a diagnostic of the properties of different components of young stellar objects. In this paper a molecular inventory for the envelopes around a sample of low-mass protostars is presented. Compared to previous studies this is the first substantial study of the chemical composition of a significant sample of low-mass protostars. These objects have formed a central protostar, but are still deeply embedded in their envelope and represent the first stage after the collapse of the dark cloud cores. Such objects differ from the pre-stellar cores for which chemical studies have previously been performed by, e.g., Bergin et al. (2001), Tafalla et al. (2002) and Lee et al. (2003), in that the central source heats the envelope and dominates the energy balance rather than, e.g., the external interstellar radiation field.

Other studies of the chemistry of low-mass protostellar objects include those in the Serpens region by Hogerheijde et al. (1999) and of specific molecules such as the sulfur-bearing species and deuterated molecules (e.g., Buckle & Fuller 2003; Roberts et al. 2002). Single objects, such as the low-mass protostar IRAS 16293-2422, have been the target of numerous studies (e.g., Blake et al. 1994; van Dishoeck et al. 1995; Ceccarelli et al. 1998; Schöier et al. 2002; Cazaux et al. 2003). This object is particularly interesting because of its rich spectrum and evidence for evaporation of ices in the inner hot regions (Ceccarelli et al. 2000a,b; Schöier et al. 2002). One of the questions that can be addressed with this study is how representative the chemistry of IRAS 16293-2422 is compared to that in other low-mass protostellar objects.

One of the major steps forward in this line of research in recent years has been the observations and analysis of the (sub)millimeter continuum emission from the dust around pre- and protostellar objects using bolometer cameras such as SCUBA on the JCMT (e.g Chandler & Richer 2000; Hogerheijde & Sandell 2000; Evans et al. 2001; Motte & André 2001; Jørgensen et al. 2002; Shirley et al. 2002; Schöier et al. 2002) and infrared extinction studies (e.g., Alves et al. 2001; Harvey et al. 2001). By fitting the radial distributions of the continuum emission and SEDs of the objects, the dust component and physical structure of the envelopes can be constrained, and, with assumptions about the gas-to-dust ratio and gas-dust temperature coupling, the physical properties of the gas in the envelope can be derived. Such physical models can then be used as the basis for determining the molecular excitation and for deriving abundances relative to H_2 by comparing to molecular line observations (e.g., Bergin et al. 2001; Jørgensen et al. 2002; Schöier et al. 2002; Tafalla et al. 2002; Lee et al. 2003).

Based on these methods it has become increasingly clear that large vari-

ations of molecular abundances can occur in protostellar environments. Examples are depletion of molecules at low temperatures due to freeze-out on dust grains (e.g., Caselli et al. 1999; Jørgensen et al. 2002; Tafalla et al. 2002) and enhancements of molecular species in warm regions where ices evaporate (Ceccarelli et al. 2000a,b; Schöier et al. 2002) or in shocked gas associated with protostellar outflows or jets (Bachiller et al. 1995; Bachiller & Pérez Gutiérrez 1997; Jørgensen et al. 2004a).

Jørgensen et al. (2002) (Chapter 2) established the physical properties of the envelopes around a sample of low-mass protostars from 1D radiative transfer modeling of SCUBA dust continuum maps. The derived density and temperature structure and size was used as input for modeling CO (sub)millimeter line emission. It was found that the CO lines could be reproduced with the physical models assuming constant fractional abundances with radius. The derived values for the envelopes with the most massive envelopes - typically interpreted as the "youngest" class 0 protostars - were found to be lower than abundances quoted for nearby dark clouds by an order of magnitude. In contrast the potentially more evolved class I objects were found to have envelopes with CO abundances closer to the dark cloud value. It was suggested that this was related to CO freezing out on dust grains at low temperatures and in dense environments.

This paper is a continuation of Chapter 2 and the analysis of the class 0 YSO, IRAS 16293-2422 presented by Schöier et al. (2002). Based mainly on JCMT and Onsala 20 m observations, abundances for a large number of molecules are derived using detailed Monte Carlo radiative transfer for the full set of pre- and protostellar objects presented in Chapter 2 with the envelope parameters derived in that paper as input. The combination of low J 3 mm observations from the Onsala telescope and higher J lines from the JCMT allows a discussion of the radial variation of the chemistry with the low J lines mainly sensitive to the outer cold part of the envelope and the high J lines to the inner dense regions. Similar analyzes for H_2CO, CH_3OH and more complex organic species, which are particularly sensitive to the innermost hot core region, are presented in separate papers (Maret et al. 2004a; Jørgensen et al. in prep.)

The paper is laid out as follows: in Sect. 3.2 the details of the observations and reduction are presented. The modeling approach is described in Sect. 3.3 and caveats and implications for the radial structure described. Relations between the different molecular species are discussed in Sect. 3.4.

3.2 Observations

3.2.1 Observational details

The principal data set forming the basis of this work was obtained with the James Clerk Maxwell Telescope (JCMT) on Mauna Kea, Hawaii[1] where 15

[1]The JCMT is operated by the Joint Astronomy Centre in Hilo, Hawaii on behalf of the parent organizations: PPARC in the United Kingdom, the National Research Council of Canada and The

sources were observed between February 2001 and February 2003. In addition archival data for 3 class I sources - L1551-I5, TMC1 and TMC1A - observed previously in a number of these settings were used.

The A3 and B3 receivers at 210-270 GHz and 315-370 GHz, respectively, were used with the digital autocorrelation spectrometer (DAS) in setups with bandwidths ranging from 125 MHz to 500 MHz with resulting resolutions of 0.1 to 0.6 km s^{-1}. Each setting was observed with on source integration times ranging from 10 to 60 minutes per mixer reaching a typical RMS (on T_A^* scale) of 0.03 to 0.05 K in 30 minutes. The pointing accuracy for the JCMT was found to be a few arcseconds. The calibration was checked by comparison to spectral line standards and was estimated to be accurate to approximately 20%, when comparing data taken in separate runs. For most sources beam switching with a chop of 180″ was used. The only exception was N1333-I4A and -I4B for which position switching to an emission-free position at (-120″, 250″) was used.

Further observations at 3 millimeter (85 to 115 GHz) were obtained with the Onsala Space Observatory 20 m telescope[2] in observing runs in March 2002 and May 2003. The entire sample was observed at Onsala in the same species, except the two ρ Ophiuchus sources L1689B and VLA1623 which are located too far south. These two sources were observed in early April 2003 at 3 mm using the Swedish-ESO Submillimeter Telescope (SEST)[3] at La Silla in Chile. Finally CS and C^{34}S spectra were taken for a few sources in November 2001 with the IRAM 30 m telescope[4] at Pico Veleta, Spain in the range 90 to 250 GHz.

In addition to the observed settings the public JCMT archive was searched for useable data and included to constrain the models together with previously published observations. All spectra were calibrated at the telescopes onto the natural antenna temperature scale, T_A^*, using the chopper-wheel method (Kutner & Ulich 1981). The spectra were corrected for the telescope beam and forward scattering efficiencies and brought onto the main beam brightness scale, $T_{\rm mb}$, by division with the appropriate main beam efficiencies, $\eta_{\rm mb}$ (or $F_{\rm eff}/B_{\rm eff}$ in the terminology adopted at the IRAM 30 m telescope). Finally a low order polynomial baseline was subtracted for each spectrum. An overview of the observed lines is given in Table 3.1.

3.2.2 Resulting spectra

Spectra of selected molecular transitions are presented in Fig. 3.1-3.4. In order to derive the line intensities, Gaussians were fitted to each line. For the few asymmetric lines the emission was integrated over $\pm$ 2 km s^{-1} from the systemic velocity of the given source. The integrated line intensities are listed

Netherlands Organization for Scientific Research

[2]The Onsala 20 m telescope is operated by the Swedish National Facility for Radio Astronomy, Onsala Space Observatory at Chalmers University of Technology.

[3]The SEST is operated by the Swedish National Facility for Radio Astronomy on behalf of the Swedish Natural Science Research Council and the European Southern Observatory.

[4]The IRAM 30 m telescope is operated by the Institut de Radio Astronomie Millimétrique, which is supported by the Centre National de Recherche Scientifique (France), the Max Planck Gesellschaft (Germany) and the Instituto Geográfico Nacional (Spain).

Table 3.1. *Summary of the observed lines.*

Molecule	Line	Frequency	Telescope
CS	2–1	97.9810	OSO, SEST
	3–2	146.9690	IRAM
	5–4	244.9356	JCMT, IRAM
	7–6	342.8830	JCMT
$C^{34}S$	2–1	96.4129	OSO, IRAM, SEST
	5–4	241.0161	JCMT
$H^{13}CO^+$	1–0	86.7543	OSO, SEST
	3–2	260.2555	JCMT
	4–3	346.9985	JCMT
DCO^+	3–2	216.1126	JCMT
N_2H^+	1–0[a]	93.1737	OSO, SEST
HCN	4–3	354.5055	JCMT
$H^{13}CN$	1–0[a]	86.3402	OSO, SEST
	3–2	259.0118	JCMT
DCN	3–2	217.2386	JCMT
HNC	1–0	90.6636	OSO, SEST
	4–3	362.6303	JCMT
CN	1–0[a]	113.4910	OSO, SEST
	3–2[a]	340.2478	JCMT
HC_3N	10–9	90.9790	OSO, SEST
SO	$2_3 - 1_2$	99.2999	OSO, SEST
	$8_7 - 7_6$	340.7142	JCMT
SO_2	$3_{1,3} - 2_{0,2}$	104.0294	OSO, SEST
	$9_{3,7} - 9_{2,8}$	258.9422	JCMT

Notes: [a]Hyperfine splitting observable.

in Tables 3.2-3.6. In case of non-detection, the 2σ upper limit is given where $\sigma = 1.2\sqrt{\Delta v\, \delta v}\, \sigma_{\rm rms}$ with Δv the expected line width (≈ 1 km s^{-1} for the observed sources/molecules), δv the channel width in the given spectral line-setup and $\sigma_{\rm rms}$ the rms noise in the observed spectra for the specific channel width. The factor 1.2 represents the typical 20% calibration uncertainty found by comparing to spectral line standards and observations from different nights.

For most sources the line profiles are quite symmetric and can be well-represented by the Gaussians: the main exceptions are the strong, optically thick HCN 4-3 and CS lines toward especially N1333-I4A and -I4B. The HCN and CS lines toward these objects seem to be dominated by outflow emission. SO_2 is only detected in the low excitation $3_{1,3} - 2_{0,2}$ line toward N1333-I4A and -I4B, and the two objects in ρ Oph, VLA1623 and L1689B. The higher excitation $9_{3,7} - 9_{2,8}$ line was also observed in a setting together with $H^{13}CN$ 3–2 but was not detected toward any source. Furthermore the high J lines of SO

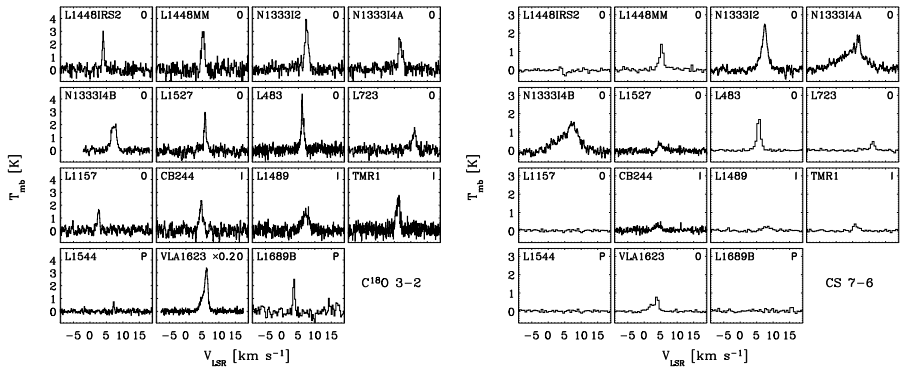

Figure 3.1. *Spectra of $C^{18}O$ $J = 3 - 2$ (left) and CS $J = 7 - 6$ (right) from JCMT observations. In this figure, and Fig. 2-3.4, the classes of the individual objects are indicated in the upper right corner of each plot by "0" for the class 0 objects (envelope mass $> 0.5 M_{\odot}$), "I" for the class I objects (envelope mass $< 0.5 M_{\odot}$) and "P" for the pre-stellar cores.*

were also only detected toward the objects in NGC 1333 and toward VLA1623, suggesting a chemical effect.

Some systematic trends can be seen from the Tables and Figures. In general the lines are significantly weaker than those found in IRAS 16293-2422 (Blake et al. 1994; van Dishoeck et al. 1995). Especially for the Class I objects in our sample (i.p., L1489 and TMR1) a number of usually quite strong lines (e.g., HCN 4–3) were not detected. The effects of the chemistry are also hinted at by comparing, e.g., the source to source variations of the HNC 4–3 and CN 3–2 spectra. An interesting effect can be seen for the deuterium-bearing species: note that the DCO^+ 3–2 lines are detected toward the pre-stellar cores but not the $H^{13}CO^+$ 3–2 lines and vice versa for the class I objects, clearly indicating a higher degree of deuteration in the colder pre-stellar cores. How much of this can be attributed to excitation and simple mass or distance effects is, however, not clear. IRAS 16293-2422 for example has the most massive envelope compared to the other class 0 objects and is also located closer than, e.g., the other massive sources in the NGC 1333 region. In contrast the class I objects by their very definition have the least massive envelopes, so the absence of lines toward some of these objects may simply reflect lower column densities for the observed species for these sources. In order to address this in more detail it is necessary to model the full line radiative transfer as was done in Jørgensen et al. (2002) and Schöier et al. (2002).

Table 3.2. *Line intensities ($\int T_{\rm MB}\,{\rm d}v$) for CS, $C^{34}S$ and SO transitions from the JCMT and Onsala 20 m telescope.*

	CS		$C^{34}S$		SO	
	5–4	7–6	2–1	5–4	$2_3 - 1_2$	$8_7 - 7_6$
L1448-I2	0.31	< 0.18	0.39	...	1.7	< 0.053
L1448-C	2.2	2.0	0.47	0.26	1.7	< 0.096
N1333-I2	4.0	4.9	IRAM[a]	0.66	2.9	1.7
N1333-I4A	7.9	4.8	IRAM[a]	1.25	7.4	5.8
N1333-I4B	6.3	4.7	IRAM[a]	0.79	6.3	1.8
L1527	1.8	0.45	IRAM[a]	< 0.061	0.42	< 0.067
VLA1623	4.3	1.6	SEST[a]	0.28	SEST[a]	0.98
L483	4.1	2.5	0.38	0.47	1.4	< 0.13
L723	4.3	0.67	0.18	0.29	1.4	< 0.12
L1157	0.93	< 0.094	0.20	< 0.075	2.1	< 0.21
CB244	1.9	0.87	0.16	< 0.12	0.87	< 0.074
L1489	0.62	0.71	< 0.040	< 0.098	0.26	< 0.083
TMR1	0.77	0.60	...	< 0.086	0.28	< 0.054
L1551	3.2	3.4	...	0.35	0.59	...
TMC1	0.46	...	...	...	0.39	...
TMC1A	0.58	...	...	...	0.12	...
L1544	< 0.14	< 0.094	0.22	...	0.82	< 0.13
L1689B	< 0.16	< 0.12	SEST[a]	< 0.028	SEST[a]	< 0.099

[a] 3 mm observations from the IRAM 30 m and SEST telscopes given in Table 3.5 and 3.6, respectively.

Table 3.3. *Line intensities ($\int T_{\rm MB}\,{\rm d}v$) for the $H^{13}CO^+$, N_2H^+, DCO^+ and DCN transitions from the JCMT and Onsala 20 m telescope.*

	$H^{13}CO^+$			N_2H^+	DCO^+	DCN
	1–0	3–2	4–3	1–0	3–2	3–2
L1448-I2	1.6	0.89	...	10.5	0.91	0.13
L1448-C	2.0	1.9	...	11.7	1.9	0.40
N1333-I2	1.8	2.1	2.7	14.2	0.95	0.46
N1333-I4A	2.3	1.4	...	15.9	3.2	0.40
N1333-I4B	2.1	0.57	...	13.5	2.0	0.31
L1527	2.2	1.1	0.47	4.4	0.70	0.10
VLA1623	SEST[a]	4.7	3.0	SEST[a]	3.6	0.43
L483	1.5	1.7	1.2	13.7	0.85	0.25
L723	0.61	0.94	0.70	4.8	0.36	< 0.064
L1157	0.89	0.61	0.52	7.3	0.64	< 0.078
CB244	0.87	0.73	0.43	6.3	0.34	< 0.083
L1489	0.96	0.82	0.61[b]	0.26	< 0.092	< 0.089
TMR1	1.1	0.51	0.20[b]	0.37	< 0.095	< 0.089
L1551	...	2.4[b]	2.2[b]	15.7	1.3	...
TMC1	...	<0.27[b]	<0.12[b]	5.8	< 0.16	...
TMC1A	...	<0.27[b]	<0.13[b]	7.1	< 0.12	...
L1544	0.92	<0.10	...	6.0	0.56	0.12
L1689B	SEST[a]	0.22	...	SEST[a]	0.55	< 0.107

[a]SEST 3 mm observations of the southern sources given in Table 3.6. [b]from Hogerheijde et al. (1997).

Table 3.4. *Line intensities ($\int T_{\rm MB}\,{\rm d}v$) for the HCN, $H^{13}CN$, HNC and CN transitions from the JCMT and Onsala 20 m telescope.*

	HCN	$H^{13}CN$		HNC		CN				
	4–3	1–0	3–2	1–0	4–3	$1_{022}-0_{011}$	$1_{023}-0_{012}$	$1_{021}-0_{011}$	$1_{022}-0_{012}$	3–2[b]
L1448-I2	1.4	0.44	<0.13	8.2	0.60	1.3	2.7	0.88	0.92	1.2
L1448-C	5.3	0.82	0.50	8.6	3.4	1.4	2.5	0.87	1.6	1.9
N1333-I2	5.3	0.59	0.62	8.9	3.3	2.5	2.8	1.1	1.7	1.5
N1333-I4A	6.6	1.5	0.65	11.6	2.8	1.9	3.0	1.2	1.8	1.1
N1333-I4B	9.6	0.96	0.70	4.4	2.0	1.8	2.5	0.88	1.2	0.73
L1527	1.4	0.43	<0.067	3.8	0.40	1.4	2.2	1.0	0.81	1.3
VLA1623	2.2	SEST[a]	<0.153	SEST[a]	2.5	——	SEST[a]	——		1.4
L483	3.5	0.69	0.52	3.7	2.2	0.63	1.4	0.46	0.99	2.4
L723	1.7	0.16	<0.080	2.8	1.3	0.28	0.51	0.21	0.31	1.1
L1157	1.1	0.23	<0.087	3.7	1.0	0.57	0.87	0.37	0.35	0.40
CB244	3.2	0.14	<0.093	3.7	0.74	0.54	0.62	0.31	0.43	1.1
L1489	0.85	0.29	<0.087	2.1	1.0	<0.14	0.63	<0.14	<0.14	0.67
TMR1	0.63	0.15	<0.15	2.3	0.33	<0.14	0.37	<0.14	<0.14	0.47
L1551	...	<0.12	...	9.0	2.97	1.4	1.8	1.2	1.1	...
TMC1	...	<0.094	...	3.2	<0.27	0.63	0.72	0.82	0.30	...
TMC1A	...	<0.092	...	3.8	0.29	0.55	0.79	0.49	0.49	...
L1544	<0.12	0.70	<0.11	4.0	0.35	0.56	0.90	0.44	0.65	0.21
L1689B	<0.11	SEST[a]	<0.10	SEST[a]	<0.24	——	SEST[a]	——		<0.092

Notes: [a]SEST 3 mm observations of the southern sources given in Table 3.6. [b]Hyperfine components blended.

Table 3.5. *Line intensities ($\int T_{\rm MB}\,{\rm d}v$) for CS and $C^{34}S$ transitions from the IRAM 30 m telescope.*

	CS		$C^{34}S$
	3–2	5–4	2–1
L1448-C	2.7	2.9	0.45
N1333-I2	6.2	9.4	1.3
N1333-I4A	11.7	15.1	1.6
N1333-I4B	6.7	10.3	0.73
L1527	...[a]	1.8	0.11

Notes: [a] 2σ upper limit of $C^{34}S$ 3–2 intensity of 0.064 K km s^{-1}.

Table 3.6. *Line intensities ($\int T_{\rm MB}\,{\rm d}v$) for the 3 mm observations of the southern sources from the SEST.*

		VLA1623	L1689B
CN	$1_{022} - 0_{011}$	0.73	0.13
	$1_{023} - 0_{012}$	1.2	0.20
	$1_{021} - 0_{011}$	0.70	0.16
	$1_{022} - 0_{012}$	0.81	0.15
$C^{34}S$	2–1	0.41	0.33
$H^{13}CO^+$	1–0	3.1	1.2
$H^{13}CN$	1–0	0.98	0.10
HC_3N	10–9	0.38	0.052
HNC	1–0	1.5	1.1
N_2H^+	1–0	8.0	6.0
SO	$2_3 - 1_2$	3.1	2.9

3.3 Modeling

3.3.1 Constant abundances in static models

To model the chemical abundances the same approach as in Chapter 2 and Schöier et al. (2002) was adopted: the physical structure for each individual source presented in Chapter 2 was used as input for calculating the molecular excitation and the detailed radiative transfer using the Monte Carlo code of Hogerheijde & van der Tak (2000). This code agrees within the Monte Carlo noise with the code of Schöier et al. (2002) that was used to derive the abundances for IRAS 16293-2422. Both codes were furthermore benchmarked by van Zadelhoff et al. (2002) together with other line radiative transfer codes. The same molecular data as in Schöier et al. (2002) were used. These are sum-

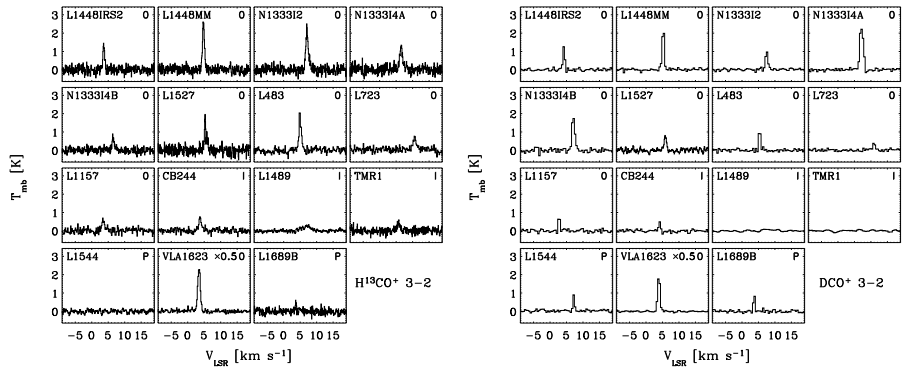

Figure 3.2. *Spectra of $H^{13}CO^+$ (left) and DCO^+ $J = 3 - 2$ (right) from JCMT observations.*

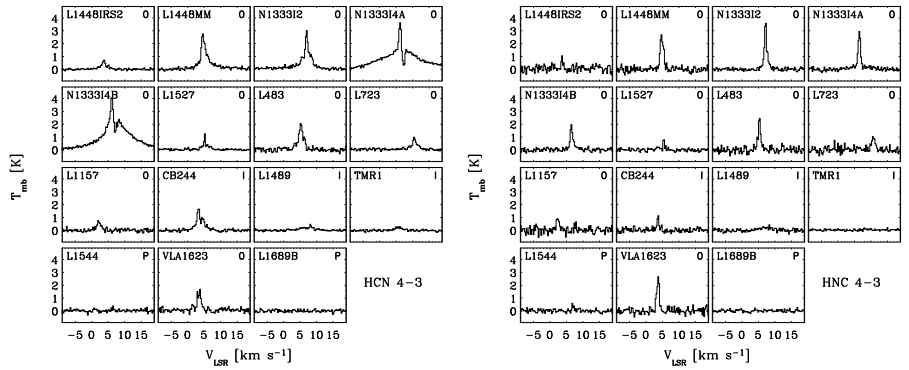

Figure 3.3. *Spectra of HCN (left) and HNC (right) $J = 4 - 3$ from JCMT observations.*

marized in the database of Schöier et al. (in prep.).

A few species, e.g., CN and N_2H^+, show clear hyperfine splitting of the lines. For the CN 1–0 line the individual hyperfine components can easily be disentangled (see Fig. 3.4) and each of these can be modeled as separate lines with individual excitation rates. In general the model fits the individual hyperfine components well, although in the poorest fits the strongest hyperfine component is overestimated in the modeling. For the CN 3–2 lines at 340.248 GHz three hyperfine components are overlapping. These transitions are optically thin, however, and can therefore be modeled as one line. For N_2H^+ molecular data only exist for the main rotational transitions. Again this does not pose a problem if the emission is optically thin. For the 1–0 transition this is true for most sources as also indicated by the observed ratios of their hyperfine components.

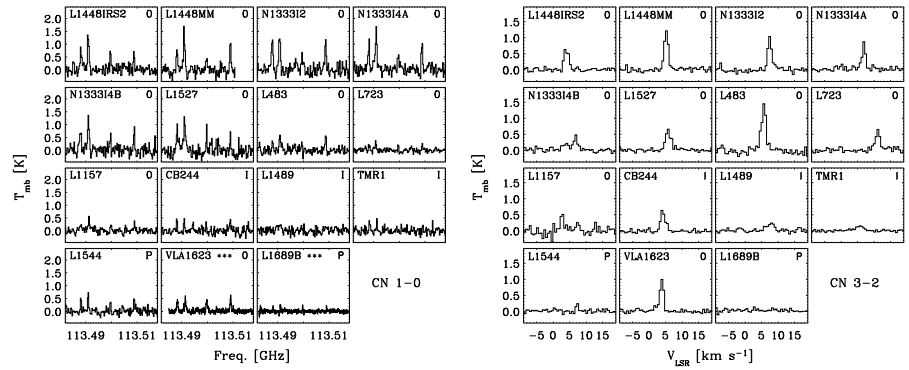

Figure 3.4. *Spectra of CN $J = 1 - 0$ (left) and $J = 3 - 2$ (right). The $J = 1 - 0$ observations are from the Onsala 20 m telescope and the SEST (marked with ***), the $J = 3 - 2$ observations are from the JCMT.*

For a given line the resulting sky brightness distribution was convolved with the appropriate beam and the resulting spectrum compared to the observed one. The envelope was assumed to be static and the integrated line intensity and line width fitted by varying the abundance profile and turbulent line broadening. In the first iteration, a constant fractional abundance of each molecule relative to H_2 was assumed. It is found that most lines are fitted well with such a description, except for some of the low J 3 mm lines. Abundance jumps, e.g., due to evaporation of ice mantles as found for IRAS 16293-2422, are not excluded by the present observations. However, the region where the ice mantles would evaporate (T $\gtrsim$ 90 K) is typically less than 100 AU ($\approx$ 0.5-1″) for our sources, and therefore heavily diluted in the beam. Furthermore, the lines presented in this study are predominantly sensitive to the material at low to intermediate temperatures in the envelope.

Tables 3.7-3.13 list abundances together with the number of observed lines and the reduced χ^2 for each individual source for species for which more than one line was observed. A summary of the abundances for all molecules assuming standard isotope ratios (Table 3.14) is given in Table 3.15. In each of these tables the abundances were taken to be constant over the entire extent of the envelope.

For a range of the molecules (especially CS and HCO^+) the main isotopes are not well suited for determining chemical abundances since the lines rapidly become optically thick. Moreover the emission from these species in the envelope is in some cases hard to disentangle, since the line profiles show clear signs of wing emission due to outflows and asymmetries attributed to infalling motions (Gregersen et al. 1997, 2000; Ward-Thompson & Buckley 2001). The lines from the weaker isotopes (e.g., $C^{34}S$ and $H^{13}CO^+$), however, usually do not suffer from these problems and were therefore used to constrain the abun-

Table 3.7. *Inferred abundances for CS and $C^{34}S$ and reduced χ^2 where applicable.*

Source	Abundance	$\chi^2_{\rm red}$	$n_{\rm lines}$[a]	Lines[b]
		CS		
L1448-I2	4.3×10^{-11}	...	1	5–4 (JCMT)
L1448-C	2.5×10^{-9}	2.6	2	5–4, 7–6 (JCMT)
N1333-I2	1.3×10^{-9}	0.91	2	5–4[c], 7–6[c] (JCMT)
N1333-I4A	4.7×10^{-10}	0.019	2	5–4[c], 7–6[c] (JCMT)
N1333-I4B	2.5×10^{-9}	1.1	2	5–4[c], 7–6[c] (JCMT)
L1527	3.0×10^{-9}	2.9	4	5–4, 7–6 (JCMT, CSO[d])
VLA1623	2.6×10^{-9}	2.6	2	5–4, 7–6 (JCMT)
L483	1.5×10^{-9}	1.7	2	5–4, 7–6 (JCMT)
L723	1.3×10^{-9}	13[e]	2	5–4 (JCMT), 7–6 (JCMT)
L1157	1.9×10^{-10}	...	1+(1)	5–4 (JCMT), 7–6 (JCMT; nd)
CB244	4.0×10^{-9}	0.22	2	5–4, 7–6 (JCMT)
L1551	4.1×10^{-10}	0.64	4	5–4, 7–6 (JCMT, CSO[d])
L1489	2.8×10^{-9}	2.7	4	5–4, 7–6 (JCMT, CSO[d])
TMR1	1.0×10^{-8}	3.2	4	5–4, 7–6 (JCMT, CSO[d])
TMC1	6.5×10^{-9}	7.6	2	5–4 (JCMT), 7–6 (CSO[d])
TMC1A	4.9×10^{-10}	1.9	2	5–4 (JCMT), 7–6 (CSO[d])
L1544	$<2.5\times10^{-10}$	...	1	5–4 (JCMT)
L1689B	$<3.0\times10^{-10}$	...	1	5–4 (JCMT)
		$C^{34}S$		
L1448-I2	4.1×10^{-11}	...	1	2–1 (OSO)
L1448-C	1.1×10^{-10}	1.6	3	2–1 (OSO, IRAM), 5–4 (JCMT)
N1333-I2	1.4×10^{-10}	0.50	2	2–1 (IRAM), 5–4 (JCMT)
N1333-I4A	4.6×10^{-11}	0.10	2	2–1 (IRAM), 5–4 (JCMT)
N1333-I4B	5.5×10^{-11}	4.1	2	2–1 (IRAM), 5–4 (JCMT)
L1527	1.5×10^{-11}	...	1+(1)	2–1 (IRAM), 5–4 (JCMT ; nd)
VLA1623	1.8×10^{-10}	3.0	2	2–1 (SEST), 5–4 (JCMT)
L483	3.1×10^{-11}	9.2	2	2–1 (OSO), 5–4 (JCMT)
L723	1.0×10^{-10}	2.7	2	2–1 (OSO), 5–4 (JCMT)
L1157	3.7×10^{-11}	...	1+(1)	2–1 (OSO), 5–4 (JCMT ; nd)
CB244	7.2×10^{-11}	...	1+(1)	2–1 (OSO), 5–4 (JCMT ; nd)
L1551	3.7×10^{-11}	...	1	5–4 (JCMT)
L1489	$<1.1\times10^{-10}$	...	(2)	2–1 (OSO; nd), 5–4 (JCMT; nd)
TMR1	$<7.9\times10^{-10}$	...	(1)	5–4 (JCMT; nd)
L1544	3.9×10^{-11}	...	1	2–1 (OSO)
L1689B	1.2×10^{-10}	...	1	2–1 (SEST)

[a]Number of observed lines; number in parentheses indicate number of lines not detected. [b]Observed lines; lines not detected indicated by "nd". [c]Complex line profile - intensity defined as line integrated over ±2 km s^{-1} relative to systemic velocity. [d]CSO line intensities from Moriarty-Schieven et al. (1995). [e]The 7–6 line alone corresponds to an abundance of 5×10^{-10}, the 5–4 line taken alone to 4×10^{-9}. The latter is in agreement with the results from modeling of the $C^{34}S$ lines.

Table 3.8. *Inferred abundances for SO and reduced χ^2 where applicable.*

Source	Abundance	$\chi^2_{\rm red}$	$n_{\rm lines}$	Lines
L1448-I2	7.0×10^{-10}	...	1+(1)	2_3–1_2 (OSO), 8_7–7_6 (JCMT ; nd)
L1448-C	1.4×10^{-9}	...	1+(1)	2_3–1_2 (OSO), 8_7–7_6 (JCMT ; nd)
N1333-I2	3.4×10^{-9}	1.3	2	2_3–1_2 (OSO), 8_7–7_6 (JCMT)[b]
N1333-I4A	4.6×10^{-9}	0.66	2	2_3–1_2 (OSO), 8_7–7_6 (JCMT)[b]
N1333-I4B	3.0×10^{-9}	0.82	2	2_3–1_2 (OSO), 8_7–7_6 (JCMT)[b]
L1527	1.4×10^{-10}	1.4	2+(1)	2_3–1_2 (OSO), 4_3–3_2 (NRAO[a]), 8_7–7_6 (JCMT; nd)
VLA1623	1.2×10^{-8}	1.6	3	2_3–1_2, 6_5-5_4 (SEST), 8_7–7_6 (JCMT)
L483	2.9×10^{-10}	...	1+(1)	2_3–1_2 (OSO), 8_7–7_6 (JCMT; nd)
L723	2.4×10^{-9}	...	1+(1)	2_3–1_2 (OSO), 8_7–7_6 (JCMT; nd)
L1157	1.6×10^{-9}	0.25	3+(1)	2_3–1_2 (OSO), 2_2–1_1, 43–3_2 (NRAO[a]), 8_7–7_6 (JCMT; nd)
CB244	9.0×10^{-10}	3.1	3+(1)	2_3–1_2 (OSO), 2_2–1_1, 43–3_2 (NRAO[a]), 8_7–7_6 (JCMT; nd)
L1551	1.9×10^{-10}	0.95	2	2_3–1_2 (OSO), 4_3–3_2 (NRAO[a])
L1489	2.0×10^{-9}	...	1+(1)	2_3–1_2 (OSO), 8_7–7_6 (JCMT; nd)
TMR1	4.1×10^{-9}	...	1+(1)	2_3–1_2 (OSO), 8_7–7_6 (JCMT; nd)
TMC1A	2.3×10^{-10}	...	1	2_3–1_2 (OSO)
TMC1	4.1×10^{-9}	0.70	2	2_3–1_2 (OSO), 4_3–3_2 (NRAO[a])
L1544	4.8×10^{-10}	...	1+(1)	2_3–1_2 (OSO), 8_7–7_6 (JCMT; nd)
L1689B	2.6×10^{-9}	3.3	2+(1)	2_3–1_2, 6_5-5_4 (SEST), 8_7–7_6 (JCMT; nd)

[a] 2_2-1_1 and 4_3-3_2 NRAO observations from Buckle & Fuller (2003); see further discussion in text. [b] 8_7–7_6 line very wide; larger uncertainty in derived abundance.

Table 3.9. *Inferred abundances for SO_2 based on observations of the $3_{1,3} - 2_{0,2}$ line from the Onsala 20m and SEST telescopes.*

Source	Abundance
L1448-I2	$<6.3\times10^{-11}$
L1448-C	$<2.2\times10^{-10}$
N1333-I2	$<2.5\times10^{-10}$
N1333-I4A	1.8×10^{-10}
N1333-I4B	6.6×10^{-10}
L1527	$<2.4\times10^{-10}$
VLA1623	1.7×10^{-9}
L483	$<5.3\times10^{-11}$
L723	$<1.3\times10^{-10}$
L1157	$<8.4\times10^{-11}$
CB244	$<1.0\times10^{-10}$
L1489	$<2.3\times10^{-9}$
L1544	$<9.0\times10^{-11}$
L1689B	6.3×10^{-10}

dances where detected.

Table 3.10. *Inferred abundances for $H^{13}CO^+$ and reduced χ^2 where applicable.*

Source	Abundance	$\chi^2_{\rm red}$	$n_{\rm lines}$	Lines
L1448-I2	$9.9\times10^{-12,a}$	...	1	3–2 (JCMT)
L1448-C	1.3×10^{-10}	0.21	4	1–0 (OSO), 3–2 (JCMT, CSO[b]), 4–3 (CSO[b])
N1333-I2	$4.5\times10^{-11,a}$	0.59	4	3–2 (JCMT, CSO[b]), 4–3 (JCMT, CSO[b])
N1333-I4A	$6.1\times10^{-12,a}$	1.2	3	3–2 (JCMT, CSO[b]), 4–3 (CSO[b])
N1333-I4B	$8.8\times10^{-12,a}$	2.7	2+(1)	3–2 (JCMT, CSO[b]), 4–3 (CSO[b]; nd)
L1527	8.5×10^{-12}	0.41	5	1–0 (OSO), 3–2 (JCMT, CSO[b]), 4–3 (JCMT, CSO[b])
VLA1623	$2.2\times10^{-10,a}$	2.0	3	3–2 (JCMT, CSO[b]), 4–3 (JCMT)
L483	2.8×10^{-11}	0.63	4	1–0 (OSO), 3–2 (JCMT, CSO[b]), 4–3 (JCMT)
L723	5.8×10^{-11}	0.61	3	1–0 (OSO), 3–2, 4–3 (JCMT)
L1157	$8.4\times10^{-12,a}$	0.29	2	3–2 (JCMT), 4–3 (JCMT)
CB244	7.3×10^{-11}	0.53	3	1–0 (OSO), 3–2, 4–3 (JCMT)
L1551	2.3×10^{-11}	1.3	2	3–2, 4–3 (JCMT)
L1489	$2.5\times10^{-10,a}$	...	1	3–2 (JCMT)
TMR1	$3.9\times10^{-10,a}$	...	1	3–2 (JCMT)
TMC1	$<1.4\times10^{-10,c}$	...	2	3–2, 4–3 (JCMT[c])
TMC1A	$<1.1\times10^{-11,c}$	...	2	3–2, 4–3 (JCMT[c])
L1544	$5.6\times10^{-12,a}$	...	1+(1)	3–2 (CSO[b], JCMT; nd)
L1689B	$1.7\times10^{-11,a}$	0.20	2	3–2 (CSO[b], JCMT)

[a]Fits including 1–0 line intensities given in Table 3.11. See also discussion in text. [b]CSO measurements from Gregersen et al. (1997, 2000); Gregersen & Evans (2000) - except the 4–3 line towards N1333-I2 (Blake, priv. comm.). [c]Upper limits on line intensities from Hogerheijde et al. (1997). Using their HCO^+ main isotope 3–2 and 4–3 line intensities, HCO^+ abundances of 4.7×10^{-9} and 2.2×10^{-10} are found for TMC1 and TMC1A, respectively.

Table 3.11. *Inferred abundances for $H^{13}CO^+$ including the full set of lines.*

Source	Abundance	$\chi^2_{\rm red}{}^a$	$I_{\rm obs}{}^b$	$I_{\rm mod}{}^c$
L1448-I2	1.1×10^{-11}	15	1.58	0.34
N1333-I2	4.5×10^{-11}	1.6	1.77	0.96[d]
N1333-I4A	6.5×10^{-12}	6.6	2.32	0.38
N1333-I4B	9.4×10^{-12}	9.4	2.10	0.40
VLA1623	2.2×10^{-10}	4.1	3.09	1.76
L1157	9.2×10^{-12}	8.1	0.89	0.17
L1489	3.1×10^{-10}	6.0	0.96	0.44
TMR1	4.7×10^{-10}	9.4	1.13	0.40
L1544	6.7×10^{-12}	16	0.92	0.17
L1689B	1.8×10^{-11}	6.9	1.24	0.41

[a]Reduced χ^2 including lines from Table 3.10 together with 1–0 lines from the Onsala 20 m telescope or SEST. [b]Observed 1–0 line intensity ($\int T_{\rm MB}\,{\rm d}v$). [c]Modeled 1–0 line intensity ($\int T_{\rm MB}\,{\rm d}v$) with abundance from Table 3.10. [d]See also discussion in Jørgensen et al. (2004b).

Table 3.12. *Inferred abundances for $H^{13}CN$ and reduced χ^2 where applicable.*

Source	Abundance	$\chi^2_{\rm red}$	$n_{\rm lines}$	Lines
L1448-I2	2.1×10^{-11}	...	1	1–0 (OSO), 3–2 (JCMT; nd)
L1448-C	9.0×10^{-11}	2.5	2	1–0 (OSO), 3–2 (JCMT)
	7.7×10^{-11}	...	1	3–2 (JCMT)
N1333-I2	2.5×10^{-11}	7.1	2	1–0 (OSO), 3–2 (JCMT)
	2.9×10^{-11}	...	1	3–2 (JCMT)
N1333-I4A	5.6×10^{-12}	18	2	1–0 (OSO), 3–2 (JCMT)
	5.1×10^{-12}	...	1	3–2 (JCMT)
N1333-I4B	3.2×10^{-11}	1.9	2	1–0 (OSO), 3–2 (JCMT)
	2.8×10^{-11}	...	1	3–2 (JCMT)
L1527	3.2×10^{-11}	...	1	1–0 (OSO), 3–2 (JCMT; nd)
VLA1623	2.5×10^{-10}	...	1+(1)	1–0 (SEST), 3–2 JCMT; nd)
L483	2.4×10^{-11}	1.0	2	1–0 (OSO), 3–2 (JCMT)
	2.9×10^{-11}	...	1	3–2 (JCMT)
L723	3.6×10^{-11}	...	1	1–0 (OSO), 3–2 (JCMT; nd)
L1157	2.0×10^{-11}	...	1	1–0 (OSO), 3–2 (JCMT; nd)
CB244	3.1×10^{-11}	...	1	1–0 (OSO), 3–2 (JCMT; nd)
L1489	$<1.7\times10^{-10}$	...	(2)	1–0 (OSO; nd), 3–2 (JCMT; nd)
TMR1	3.7×10^{-10}	...	1+(1)	1–0 (OSO), 3–2 (JCMT; nd)
L1544	7.1×10^{-11}	...	1+(1)	1–0 (OSO), 3–2 (JCMT; nd)
L1689B	1.3×10^{-11}	...	1+(1)	1–0 (SEST), 3–2 (JCMT ; nd)

See description in Table 3.7.

Table 3.13. *Inferred abundances for CN using the 1–0 hyperfine transitions and reduced χ^2 where applicable.*

Source	Abundance	$\chi^2_{\rm red}$	$n_{\rm lines}$
L1448-I2	8.3×10^{-10}	0.13	4
L1448-C	2.4×10^{-9}	2.4	4
N1333-I2	2.4×10^{-9}	2.3	4
N1333-I4A	6.1×10^{-10}	1.4	4
N1333-I4B	8.6×10^{-10}	1.5	4
L1527	1.6×10^{-9}	0.93	4
VLA1623	3.5×10^{-9}	2.0	4
L483	3.3×10^{-10}	2.3	4
L723	7.2×10^{-10}	1.8	4
L1157	5.1×10^{-10}	1.1	4
CB244	1.0×10^{-9}	3.7	4
L1551	1.1×10^{-9}	3.6	4
L1489	4.6×10^{-9}	...	1+(3)
TMR1	5.0×10^{-9}	...	1+(3)
TMC1	1.3×10^{-8}	5.1	4
TMC1A	2.1×10^{-9}	3.0	4
L1544	6.8×10^{-10}	1.7	4
L1689B	1.6×10^{-10}	3.9	4

3.3.2 Shortcomings of the models; drop abundance profiles

For a number of species the constant fractional abundance model gives poor results ($\chi^2 \gtrsim 5$) when fitting both the lowest rotational lines from the Onsala 20 m and higher excitation lines from the JCMT. A similar trend was seen in modeling of the CO isotopic species in Paper I, where the 1–0 lines were typically underestimated in models fitted to the 2–1 and 3–2 lines. This trend is particularly pronounced for $H^{13}CO^+$ and the nitrogen-bearing species (HCN, $H^{13}CN$, CN and HNC), whereas the low J lines of CS, for example, can be fitted well by a constant abundance. This may be due to the critical density of the observed transitions which should be compared to the typical freeze-out and desorption timescales for the given densities and temperatures. Fig. 3.5 shows the density for two objects, N1333-I2 and TMR1, as function of temperature (i.e., depth) compared to the critical densities of various transitions of CS, CO, HCO^+ and HCN (e.g., Jansen 1995) for the same temperatures. Since the critical densities of the CS/$C^{34}S$ 2–1 lines are higher than those of the HCO^+ and CO 1–0 lines, CS is less sensitive to the outer region of the envelope where depletion and contribution from the surrounding cloud may be important. This may explain why these transitions can be modeled in the constant abundance framework. The observed 4–3 transitions of, i.p., HCN and HNC have the highest critical densities and these lines therefore probe the innermost part of the envelope.

In the outer regions of the envelope the depletion timescale for CO is comparable to the lifetime of the protostars ($\sim 10^4 - 10^5$ years) at the temperatures where the molecule can freeze-out. This could explain the failure of the constant abundance models in describing the lowest J lines for CO (and thereby also HCO^+; see discussion in Sect. 3.4.3): in prestellar cores (e.g Caselli et al. 1999; Tafalla et al. 2002) a trend is seen of decreasing CO abundances with increasing density toward the center. Since the temperature in the bulk of the material in these objects is low enough for CO to be frozen out, the explanation for the radial dependence is a difference in density and thus the freeze-out timescale. Therefore the time for CO to freeze-out in the outermost regions may simply be too long to result in appreciable amounts of depletion. For the protostellar cores the difference is the heating by the central source, which induces a temperature gradient toward the center. CO is therefore expected to be frozen out in a small region, where the density is high enough that the freeze-out timescale is short, yet the temperature low enough that CO is not returned to the gas-phase.

A simple way of testing this can be performed by introducing a "drop" chemical structure as illustrated in Fig. 3.6, with a constant undepleted CO abundance X_0 in the parts of the envelope with densities lower than $3\times10^4\,\mathrm{cm}^{-3}$ or temperatures higher than 30 K. A lower CO evaporation temperature of $\sim$ 20 K is ruled out by the 3–2 line intensities (Chapter 2). The undepleted abundance, X_0, is taken to be the same in the inner and outer regions of the envelope to avoid adding another free parameter. The abundance in the region

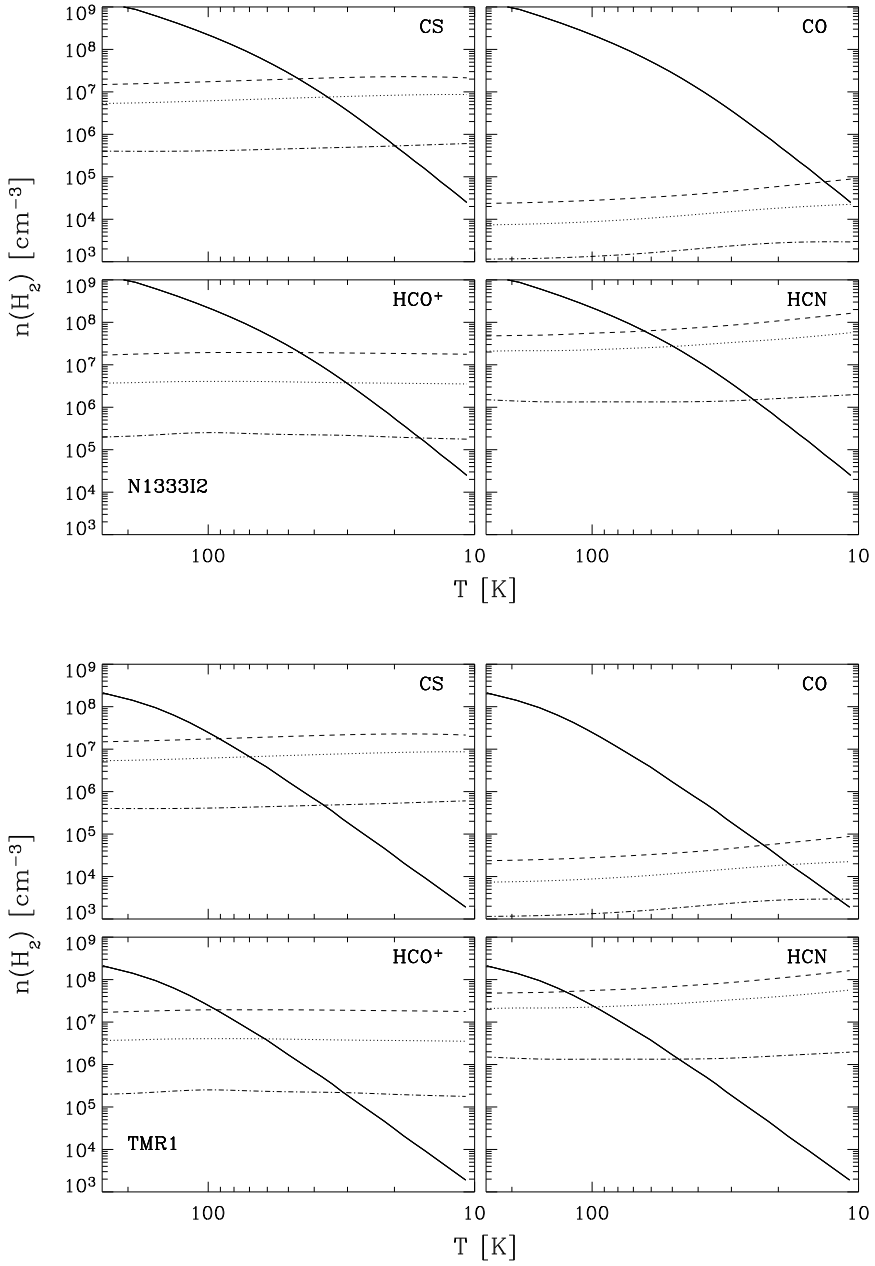

Figure 3.5. *Density as function of temperature for the envelopes around TMR1 and N1333-I2 (solid line) compared to the critical densities of the observed transitions of CS, CO, HCO^+ and HCN. The critical densities are indicated in order of increasing excitation by the dashed-dotted, dotted and dashed lines, respectively, i.e., showing the 2–1, 5–4 and 7–6 transitions for CS, the 1–0, 2–1 and 3–2 transitions for CO, and the 1–0, 3–2 and 4–3 transitions for HCO^+ and HCN.*

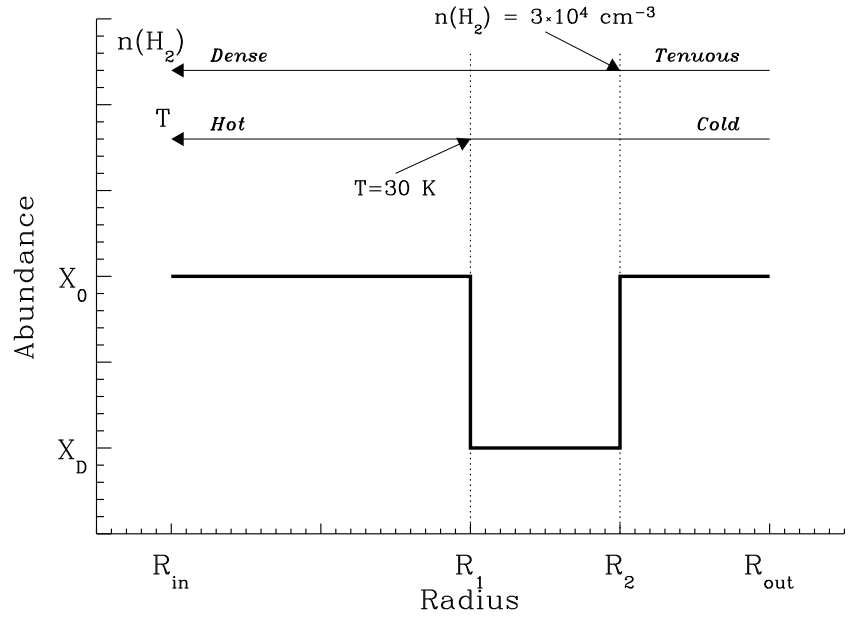

Figure 3.6. *Simulated abundance profile in "drop" models.*

with temperatures lower than 30 K and densities higher than $3 \times 10^4\,\mathrm{cm}^{-3}$, X_D, can then be adjusted to fit the observations.

Fig. 3.7 shows a comparison for L723 between the models with a constant fractional abundance from Paper I and a model with two abundance jumps described above. The latter model has two free parameters (besides the Doppler broadening, which does not alter the results), X_0 and X_D. In the constant abundance model, the $C^{18}O$ abundance is 3.9×10^{-8}, while in the "drop" model, the undepleted abundance X_0 is 2×10^{-7} and the depleted abundance X_D is 2×10^{-8}. Similar fits to the $C^{18}O$ abundances of one of the class I objects, L1489, provide equally good results - again allowing the 1–0 lines to be fitted together with the 2–1 and 3–2 lines. The fitted abundances in the case of L1489 are X_0 of 5×10^{-7} and X_D of 5×10^{-8}.

The fact that the 1–0, 2–1 and 3–2 lines can all be fitted in the drop models is not unexpected since an extra free parameter is introduced compared to the results presented in Chapter 2, which is used to fit only one extra line. Still, it should be emphasized that the chemical structure in the drop models has its foundation in results from the pre-stellar cores and is thus not completely arbitrary. As expected, the constant fractional abundances found for both L723 and L1489 in Chapter 2 are a weighted average of X_D and X_0 from the drop models. While the constant abundances were significantly different for L723 and L1489 (1.9×10^{-5} and 1.0×10^{-4}, respectively), those in the drop models are

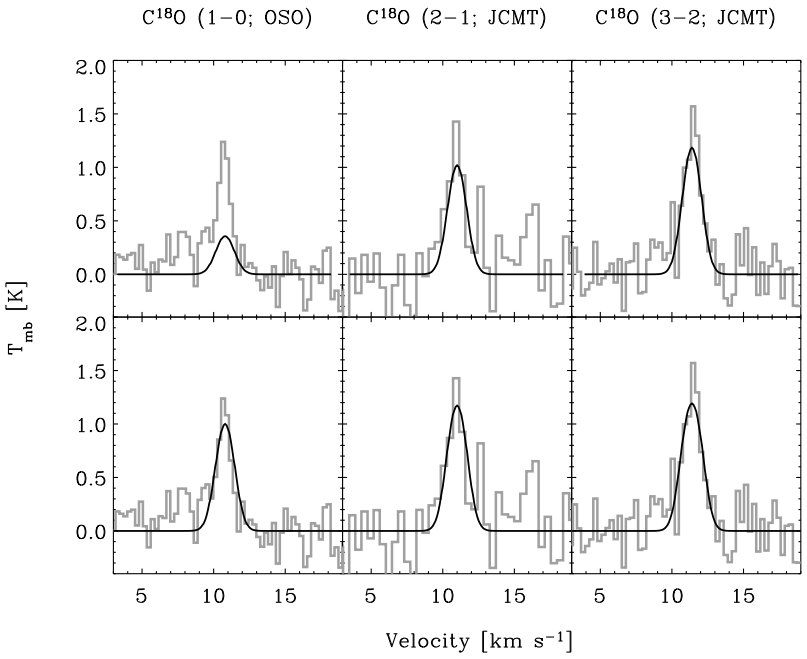

Figure 3.7. *Fitted $C^{18}O$ line-profiles for L723. Upper panels: constant fractional abundance of 3.9×10^{-9} from Paper I. Lower panels: drop model with abundances of X_0=2.0×10^{-7} for the undepleted material (with either temperatures higher than 30 K or densities lower than 3×10^{-4}) and an abundance of $X_{\rm D}$=1.5×10^{-8} for material with CO frozen out.*

more similar: the factor 2.5 difference in derived abundances can be explained through the uncertainties and approximations in the physical and chemical description.

Besides these limitations, the constant fractional abundances characterize the overall envelope chemistry as a good first-order approximation. The more general trends in abundance variation from source-to-source can thereby be used for a statistical comparison with the caveat that the selected transitions may be probing different temperature and density regimes in which the chemistry may vary. It is important to note that none of the abundances are correlated with the distances to the sources or the slopes of their density profiles, indicating that the uncertainties in these parameters do not introduce signficant systematic errors.

VLA1623 shows high abundances of most molecular species compared to the average class 0 objects. As mentioned in Paper I the envelope model of this particular object is highly uncertain since it is located in a dense ridge of

material and molecular tracers with low critical densities, in particular the CO lines and the low J 3 mm transitions of the other species, may be sensitive to this component rather than the envelope itself.

TMC1A stands out among the remainder of the class I objects with significantly lower abundances in all molecules. Hogerheijde et al. (1998) likewise found that the envelope mass estimated through 1.1 mm continuum observations was a factor 5 higher than the mass estimated on the basis of ^{13}CO, C^{18}O and HCO$^+$ measurements. One possibility is that TMC1A does have a more massive envelope and thus lower abundances due to depletion such as seen for CO in Chapter 2. Alternatives could be that the density in the envelope of this object has been overestimated from the models of the dust continuum emission or that the molecular line emission is tracing material not directly associated with the bulk material in the protostellar envelope.

This could be a general problem for more sources: are there systematic errors of the envelope dust mass leading to false trends in abundances? A systematic overestimate of the mass (i.e., density) for the class 0 objects would lead to systematically lower abundances, similar to the depletion effects observed for CO in Chapter 2. On the other hand a change in abundance as seen, e.g., for CO, would require that the density scale for the class 0 objects is off by approximately an order of magnitude, and the submillimeter dust emission and molecular lines would have to trace quite unrelated components. This is contradicted by the relative success of the models in simultaneously explaining observations of both line and continuum emission from single-dish telescopes (Chapter 2, Schöier et al. 2002, this paper) and higher resolution interferometers (Jørgensen et al. 2004b; Schöier et al. 2004a).

3.3.3 Effect of velocity field

Most observed lines are simple Gaussians with typical widths of 1 km s^{-1} (FWHM). Still, for some molecules significant variations are found between the widths for different rotational transitions and thereby the broadening due to systematic and/or turbulent motions required to model the exact line profiles. This indicates either systematic infall in the envelope as expected from the line profiles of some of the optically thick species or a variation of the turbulent velocity field with radius.

The problem with the current models is that the power-law density profile adopted in Chapter 2 does not give direct information about the velocity field, as would be obtained by fitting a specific collapse model like the inside-out collapse model by Shu (1977). A velocity field can, however, still be associated with the derived density distribution, using the mass continuity equation. This equation:

$$\frac{\partial \rho}{\partial t} + \rho \nabla \cdot \mathbf{v} = 0 \tag{3.1}$$

becomes for a spherical symmetric envelope:

$$\frac{\partial \rho}{\partial t} + \frac{1}{r^2}\frac{\partial}{\partial t}(r^2 \rho v_r) = 0 \tag{3.2}$$

where v_r is the radial velocity. Assuming $\rho \propto r^{-p}$, a power-law velocity distribution $v \propto r^{-q}$ and a static envelope density distribution ($\frac{\partial \rho}{\partial t} = 0$) results in:

$$\frac{1}{r^2}\frac{\partial}{\partial t}(r^2 r^{-p} r^{-q}) = 0 \tag{3.3}$$

or

$$r^{2-p-q} = const. \Leftrightarrow q = 2 - p \tag{3.4}$$

So for a given power-law density distribution, $n(\mathrm{H_2}) = n_0(r/r_0)^{-p}$, it is possible to introduce a corresponding power-law distribution for the velocity field, $v = v_0(r/r_0)^{-q}$. Here a characteristic infall velocity v_0 is introduced as an additional free parameter, which can be fitted by comparison of the line profiles to the turbulent linewidth.

In Fig. 3.8 such a comparison is shown for the $C^{34}S$ observations for the "typical" class 0 object, N1333-I2 (see also Jørgensen et al. 2004b). The observed line widths are seen to constrain the velocity field in terms of the combination of turbulent broadening and magnitude of the systematic velocity field. For a parameterization of the velocity field, an estimate of the mass accretion rate $\dot{M}$ can be derived from:

$$\dot{M} = 4\pi\, r_0^2\, \mu\, m_{\mathrm{H}}\, n_0\, v_0 \tag{3.5}$$

where μ is the mean molecular weight, 2.33. For N1333-I2 the upper limit on v_0 (at the inner radius, $r_0 = 23.4$ AU) of 2.5 km s^{-1}, i.e., assuming no turbulent broadening, translates to a mass accretion rate of $3{\times}10^{-5}$ $M_\odot$ yr^{-1}. This agrees with typical mass accretion rates inferred for the youngest protostars (e.g., Shu 1977; Bontemps et al. 1996; Di Francesco et al. 2001). The advantage of using the optically thin species to constrain the velocity field is that they do not suffer from confusion with, e.g., outflows, but only pick-up the bulk envelope material as illustrated by high angular resolution interferometer studies (e.g., Jørgensen et al. 2004b). On the other hand, complementary information about the velocity field is obtained from the detailed line-profiles of the optically thick, strongly self-absorbed lines, e.g., the relative strength of red- and blue peaks and the depth of the self-absorption feature (see, e.g., Evans (1999) and Myers et al. (2000) for recent reviews of this topic).

Fig. 3.9 illustrates the important point that the derived abundances do not depend critically on the adopted velocity field for optically thin species like $C^{34}S$, illustrating that the static envelope structure provides an adequate description to derive their overall chemical properties. This is in agreement with the conclusion reached in Chapter 2. Note that the confidence levels on the derived abundance in Fig. 3.9 only correspond to the calibration error. Systematic errors due to uncertainties in the adopted model, collisional data etc. are not taken into account, so the abundances derived may still be subject to uncertainties not apparent from this figure.

In summary, although systematic velocities probably exist in all envelopes besides the turbulent motions, the derived abundances do not depend critically on the detailed treatment of the velocity field as long as predominantly optically thin lines are considered, as in this paper. We will therefore for the

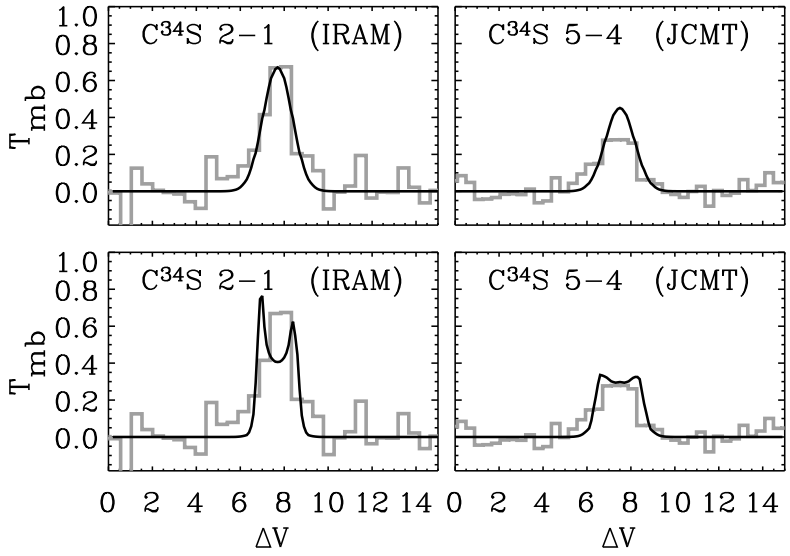

Figure 3.8. *Modeling of the velocity field in the envelope around N1333-I2: in the upper panel $C^{34}S$ model lines are compared with observations for a constant broadening of 0.8 km s^{-1}, as in Chapter 2. In the lower panel, a model with no turbulent broadening, but a power-law velocity field with $v_0 = 2.5$ km s^{-1} at the inner radius, $r_0 = 23.4$ AU, is adopted. In both plots a constant abundance of $1.4{\times}10^{-10}$ was assumed.*

remainder of this paper stick with the assumption of a non-infalling envelope with a constant turbulent broadening reproducing the approximate width of the lines.

3.4 Discussion

3.4.1 General trends and empirical correlations

A direct comparison of the derived abundances for the main isotopes can be found in Table 3.15. Where possible the abundances are calculated using the optically thin isotopic species with the standard isotopic ratios listed in Table 3.14.

In general the derived abundances vary by one to two orders of magnitude over the entire sample. Following the trend seen in Paper I of increasing abundances with decreasing envelope masses, the objects are accordingly separated into groups with envelope masses ($M_{>10\mathrm{K}}$) higher or lower than 0.5 $M_\odot$,

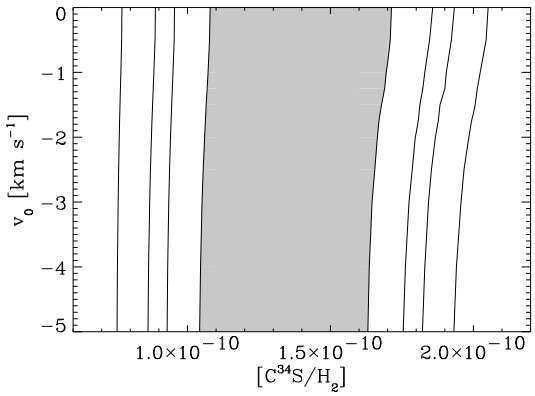

Figure 3.9. *Dependence of the $C^{34}S$ abundance on velocity field for an infalling envelope around N1333-I2. The grey region indicates 1σ confidence and the almost vertical lines indicate the 2σ, 3σ and 4σ confidence levels. It is seen that the derived abundances do not depend on the assumed velocity field for this optically thin species.*

Table 3.14. *Adopted isotope ratios.*

Isotope ratio	Value	Reference
$^{12}C/^{13}C$	70	Wilson & Rood (1994)
$^{16}O/^{18}O$	540	Wilson & Rood (1994)
$^{18}O/^{17}O$	3.6	Penzias (1981),Chapter 2[a]
$^{32}S/^{34}S$	22	Chin et al. (1996)

[a]The $^{18}O/^{17}O$ ratio is not used for the abundances derived in this paper, but was used for the CO abundances in Chapter 2 and is therefore included here for completeness.

roughly corresponding to class 0 and class I objects, respectively. This definition only moves the two borderline class 0/I objects L1551 and CB244 from class I to class 0 and vice versa compared to the source list given in Table 1 of Paper I.

On average the class 0 objects have lower abundances than the class I objects for most species (see Fig. 3.10). The most pronounced effect is seen for CO, HCO^+ and CN where the average abundances differ by up to an order of magnitude, whereas especially SO and HCN have close to constant abundances with envelope mass, albeit with large scatter around the mean. As discussed in the following sections the variations of abundances with mass are not identical, however, which indicates chemical effects regulating the relative abundances for the different molecular species. In order to quantify this more

Table 3.15. *Overview of derived abundances for main isotopic and deuterated species.*

Source	CO $\times10^{-5}$	CS $\times10^{-9}$	SO $\times10^{-9}$	HCO^+ $\times10^{-9}$	DCO^+ $\times10^{-11}$	N_2H^+ $\times10^{-9}$	HCN $\times10^{-9}$	DCN $\times10^{-11}$	HNC $\times10^{-10}$	CN $\times10^{-10}$	HC_3N $\times10^{-10}$
Class 0 (envelope mass $> 0.5M_\odot$)											
L1448-I2	0.61	0.90	0.70	0.69	0.79	>1.0	8.0	0.33	0.35	1.8	1.9
L1448-C	3.7	2.4	1.4	9.1	9.8	3.9	5.4	4.9	13	20	12
N1333-I2	2.4	3.1	3.4	3.3	1.6	5.0	2.0	2.1	1.8	3.0	4.3
N1333-I4A	0.79	1.0	4.6	0.43	1.2	>1.0	0.36	0.31	0.28	0.37	0.72
N1333-I4B	1.3	1.2	3.0	0.62	2.5	3.2	2.0	1.0	1.4	1.4	1.1
L1527	3.9	0.33	0.14	0.60	2.9	0.25	1.2	1.5	3.2	24	8.9
VLA1623	16	4.0	12	15	17	>3.0	6.6	4.7	10	8.9	3.8
L483	1.4	0.68	0.29	2.0	1.1	0.75	2.0	0.94	3.9	8.3	1.8
L723	1.9	2.2	2.4	4.1	1.6	1.3	1.0	<0.91	5.1	8.6	2.7
L1157	0.62	0.81	1.6	0.59	0.95	>1.0	0.066	<0.28	0.61	0.65	1.3
L1551-I5	3.0	0.81	0.19	1.6	1.5	3.1	...	...	0.72	...	2.1
I16293-2422[a]	3.3	3.0	4.4	1.4	1.3	0.14[b]	1.1	1.3	0.69	0.80	1.5
Class I (envelope mass $< 0.5M_\odot$)											
L1489	10	2.8	2.0	18	< 2.3	0.15	0.65	<6.4	13	22	8.7
TMR1	20	10	4.1	27	< 5.0	0.35	1.6	<15	8.1	47	35
TMC1A	2.3	0.49	0.23	0.22	< 0.65	3.9	...	...	0.38	...	100
TMC1	20	6.5	4.1	4.7	< 8.5	>1.0	...	...	<7.7	...	4.9
CB244	3.7	1.6	0.90	5.1	2.1	2.0	4.9	<1.9	7.8	20	5.9

[a]Schöier et al. (2002). [b]This paper.

Table 3.15. *(continued).*

Source	CO $\times10^{-5}$	CS $\times10^{-9}$	SO $\times10^{-9}$	HCO^+ $\times10^{-9}$	DCO^+ $\times10^{-11}$	N_2H^+ $\times10^{-9}$	HCN $\times10^{-9}$	DCN $\times10^{-11}$	HNC $\times10^{-10}$	CN $\times10^{-10}$	HC_3N $\times10^{-10}$
					Pre-stellar						
L1544	0.49	0.86	0.48	0.39	2.1	5.0	<0.35	0.77	12	4.8	16
L1689B	2.4	2.6	2.5	1.2	2.4	0.43	<0.38	<2.1	<4.6	<2.3	0.36
Averages:											
'class 0'[c]	2.1	1.5	2.0	2.2	2.3	2.5	1.3	1.4	2.8	6.9	3.5
'class I'	11	4.3	2.3	11	2.1[d]	1.6	2.1	...	7.4	30	31
Pre-stellar	1.4	1.8	1.5	0.80	2.3	2.7	< 0.36	0.77	12	4.8	8.2

[c]Excluding VLA1623. [d]Only detected for CB244.

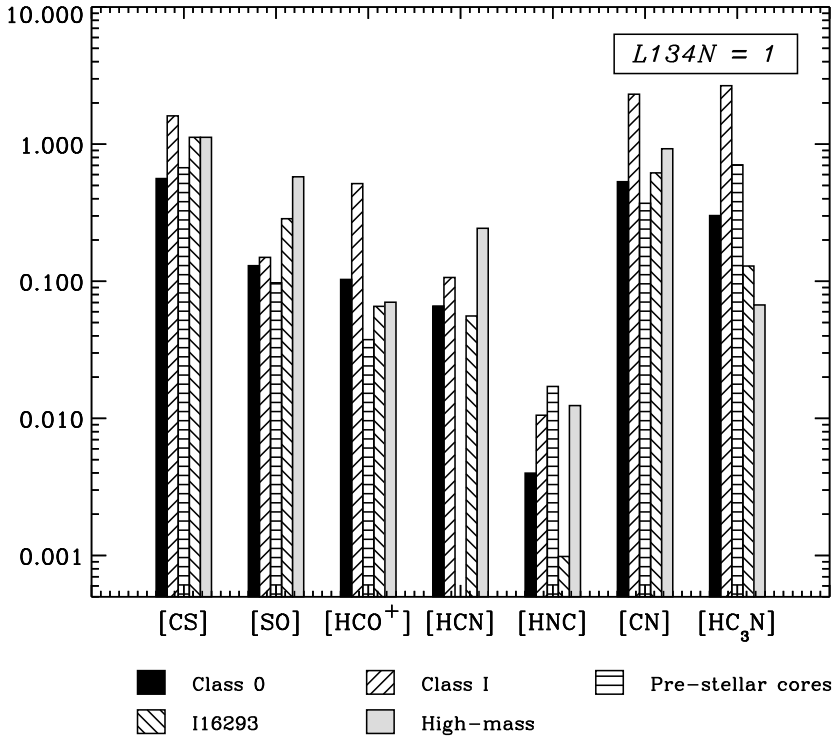

Figure 3.10. *Comparison between average abundances for class 0 and I objects and pre-stellar cores (this paper), IRAS 16293-2422 outer envelope (Schöier et al. 2002), average abundances for W3(IRS4), W3(IRS5) and W3(H2O) (all high-mass YSOs; Helmich & van Dishoeck 1997) and abundances in the dark cloud L134N (Dickens et al. 2000). Note that the L134N abundances have been rescaled assuming a CO abundance of* 2.7×10^{-4} *(Lacy et al. 1994), as was also assumed by Helmich & van Dishoeck (1997) for the high-mass YSOs. The L134N abundances thereby become: [CS] =* 2.7×10^{-9}*, [SO] =* 1.5×10^{-8}*, [HCO*$^+$*] =* 2.1×10^{-8}*, [HCN] =* 2.0×10^{-8}*, [HNC] =* 7.0×10^{-8}*, [CN] =* 1.3×10^{-9}*, and [HC*$_3$*N] =* 1.2×10^{-9}*.*

rigorously and in an unbiased way, the Pearson correlation coefficients were calculated for each set of abundances and are listed in Table 3.16. The Pearson correlation coefficient is a measure of how well a (x, y) data set is fitted by a linear correlation compared to the spread of (x, y) points. Values of ±1 indicate good correlations (with positive or negative slopes) whereas a value of 0 indicates no correlation.

As can be seen from Table 3.16, significant differences exist between the various sets of abundances. Setting an (arbitrary) cut of $> |0.7|$ to indicate good correlation, the results suggest that the molecular species are related as

Table 3.16. *Pearson correlation coefficients for the abundances for all objects.*

	CO	HCO^+	CS	SO	HCN	HNC	CN	HC_3N
Mass	-0.74	-0.51	-0.46	-0.18	-0.11	-0.40	-0.71	-0.71
CO	...	0.79	0.69	0.35	0.46	0.52	0.69	0.59
HCO^+	0.79	...	0.80	0.48	0.44	0.70	0.69	0.48
CS	0.69	0.80	...	0.79	0.29	0.48	0.31	0.39
SO	0.35	0.48	0.79	...	-0.05	0.14	-0.27	-0.03
HCN	0.46	0.44	0.29	-0.05	...	0.63	0.55	0.45
HNC	0.52	0.70	0.48	0.14	0.63	...	0.86	0.72
CN	0.69	0.69	0.31	-0.27	0.55	0.86	...	0.83
HC_3N	0.59	0.48	0.39	-0.03	0.45	0.72	0.83	...

indicated in Fig. 3.11. Individual results are shown in Fig. 3.12-3.23. The abundances of groups of species, e.g., the nitrogen- or sulfur-bearing species, are closely related as expected from naive chemical considerations. HCN is the only molecule whose abundance does not directly correlate with that of any other molecule at this level. The closest correlation is found with its isomer HNC (correlation coefficient of 0.63). The best correlation between abundance and mass is found for CO followed by CN and HC_3N. Naturally the correlations seen in this comparison may indicate the structure of the general chemical network rather than direct relations between the individual molecules: for example the ranking of correlations for SO is as follows: CS (0.79), HCO^+ (0.48) and CO (0.35). As indicated in Fig. 3.11 this is exactly the decline in correlation coefficients one would expect with the relations between these species on the pair-by-pair comparison basis adopted when constructing Fig. 3.11. Such "connectivity" could also be the cause for the relation between HNC, CN and HC_3N - the correlation between HNC and HC_3N may in fact just reflect that both these molecules are related to CN. The rather low number statistics imply that care should be taken not to overinterpret the absolute values of the correlation coefficients, but as a first step they give valuable hints. To fully understand the underlying chemistry, a more in-depth consideration on a species by species basis is required, as discussed in the following sections.

3.4.2 CS and SO

As can be seen from Fig. 3.12 abundances of the sulfur-bearing species, CS and SO, are close to constant with envelope mass, contrasting the picture for CO (Chapter 2). CS has often been used to constrain the density scales in protostellar envelopes (e.g., van der Tak et al. 2000b) assuming the chemistry to be homogeneous throughout the envelope. SO also does not show any significant trends with envelope mass, but has a larger scatter.

CS and SO are indeed found to show relatively small abundance variations

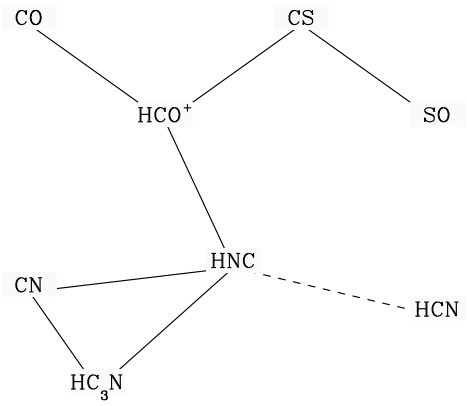

Figure 3.11. *Relations between different molecules as judged from the Pearson correlation coefficients. The dashed line between HCN and HNC indicates the strongest correlation for HCN with any of the other molecules studied. The correlation coefficient for this relation is, however, lower than the cut of 0.7 adopted for good correlations.*

in pure gas-phase models of pre-stellar cores (Bergin & Langer 1997) and in cold exterior regions of high-mass protostellar envelopes (Doty et al. 2002). As argued by Bergin & Langer (1997) and Bergin et al. (2001), however, sulfur-bearing species such as CS and SO should suffer from depletion at densities and temperatures characteristic for these regions. Maps of CS toward pre-stellar cores (Tafalla et al. 2002; Di Francesco et al. 2002) and molecular clouds (e.g., IC 5146; Bergin et al. 2001) combined with models of the abundances suggest that this molecule does indeed freeze out toward the inner colder and denser parts. Typical abundances in such environments range from $\approx 1 \times 10^{-10}$ to a few $\times 10^{-9}$ between the inner (low abundance) and outer (high abundance) regions. This agrees well with the average abundances found for the protostellar envelopes analyzed in this paper, which have a central source of heating. Our CS abundances are also similar to those inferred for a sample of high-mass protostars by van der Tak et al. (2000b) using a similar analysis.

An important conclusion regarding the derived CS abundances concerns the impact of outflow processing of the gas in the envelopes: CS and SO are seen to be greatly enhanced in shocked gas in protostellar outflows (Bachiller & Pérez Gutiérrez 1997; Jørgensen et al. 2004a). The small source-to-source variation in the derived CS abundances, however, illustrates that although increased CS abundances may be present in small parts of the envelopes, the bulk of the emission originates in parts of the envelope unaffected by such processes. The same conclusion was reached by Jørgensen et al. (2004b) from millimeter interferometer observations of the $C^{34}S$ 2–1 line emission toward

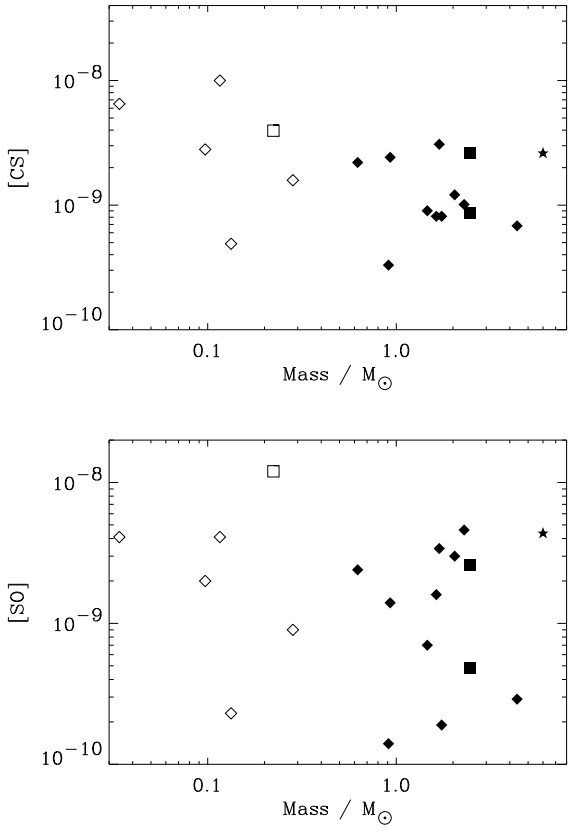

Figure 3.12. *Abundances of CS from optically thin $C^{34}S$ isotopic lines (where detected) and CS lines (upper panel) and of SO (lower panel) vs. mass. In this figure and in following figures in this paper, the class 0 objects are indicated by "⧫", the class I objects by "◊" and the pre-stellar cores by "■". The class 0 objects VLA1623 and IRAS 16293-2422 have been singled out by "□" and "★", respectively.*

NGC 1333-IRAS2.

It has been suggested that comparison between sulfur-bearing species like SO and CS can be used as chemical probes of the evolutionary stages in star-forming regions (e.g., Ruffle et al. 1999) - both when considering high- (Charnley 1997; Hatchell et al. 1998) and low-mass stars (Buckle & Fuller 2003). The time-dependence of the sulfur-chemistry network is initiated when significant amounts of H_2S are released in the gas-phase by evaporation of grain-mantles. This is followed by formation of SO and SO_2 (through reactions with H and H_3O^+ forming S and H_3S^+ and subsequently through reactions with OH and O_2). At later times most of the sulfur is incorporated into CS, H_2CS and OCS.

In particular Buckle & Fuller (2003) estimated abundances of sulfur-bearing species from SO, SO_2 and H_2S line observations toward a sample of class 0 and I objects assuming LTE and a constant CO/H_2 abundance ratio. They found that their class I low-mass YSOs had lower abundances of SO and H_2S than class 0 objects, suggesting that this was a result of their later chemical evolutionary stage. For the sources in this paper it is seen, however, that there is no significant difference in SO abundances between class 0 and I objects. Van der Tak et al. (2003) surveyed a range of different sulfur-bearing species toward a sample of high-mass YSOs and likewise found no systematic trends between known indicators of the evolutionary stage and the abundances of the sulfur molecules.

There is a slight overlap between the objects studied by Buckle & Fuller (2003) and those treated in this paper. For these overlapping objects the Buckle & Fuller data have been included in our analysis as indicated in Table 3.8, and it is found that our models can explain their observations. A likely explanation for the different findings is therefore the CO depletion found for sources with the more massive envelopes (Paper I and Sect. 3.3.2 in this paper). In fact abundances calculated assuming a $[CO/H_2]$ abundance of 1×10^{-4} leads to overestimated abundances for objects in which CO is depleted, i.e., those with the most massive envelopes (Chapter 2). The abundances for the class 0 objects in Buckle & Fuller (2003) could therefore be overestimated and their evolutionary trend an artifact of this assumption. Fig. 3.13 compares the relation between CS and SO abundances relative to the density scale set in Paper I and to a CO abundance of 10^{-4}. Fixing the CO abundance increases the average SO and CS abundances for the class 0 objects - to almost an order of magnitude higher than those for the class I objects. This in fact resembles what Buckle & Fuller (2003) find.

An interesting feature of Fig. 3.13 is the correlation between the CS and SO abundances. Here the normalization to the CO abundance also serves as a valuable test: if for some reason the absolute density scale had been systematically overestimated for the most massive envelopes and underestimated for the least massive envelopes, a false trend of abundances with mass could result and trends between abundances such as those seen in Fig. 3.13 should arise. In this case, however, normalization by a "standard" abundance should take out such an effect, but as illustrated in Fig. 3.13 this is not the case. The relation between CS and SO therefore seems to be real.

Interestingly, the CS/SO abundance ratio has previously also been suggested to trace evolutionary effects related to cloud conditions and evolution, e.g., variation of the initial C/O ratio, density effects, the temporal evolution of a given core or importance of X-rays (Bergin et al. 1997; Nilsson et al. 2000). It is found through time dependent modeling of the chemistry that the CS/SO ratio increases throughout the evolution of a molecular cloud starting from an atomic carbon-rich phase, but stabilizes at late times at a level dependent on the initial C/O ratio. As illustrated in Fig. 3.13, the relationship between the CS and SO abundances is clearly non-linear, implying that one or more of these effects may play a role in determining the relative abundances of these

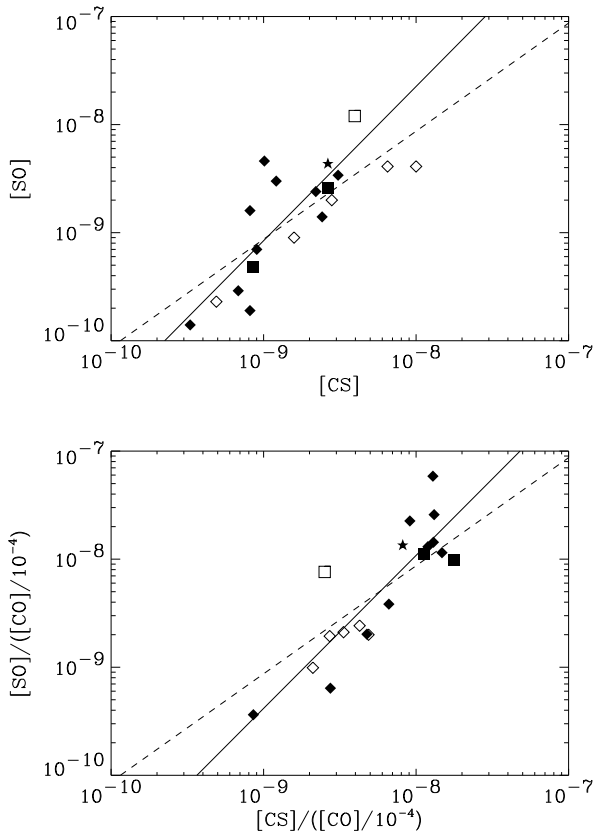

Figure 3.13. *CS vs. SO abundance. The dashed line indicates a linear relation between the CS and SO abundances, the solid line is the best-fit correlation. In the lower panel the abundances have been normalized to a CO abundance of 10^{-4}, mimicking the assumption in Buckle & Fuller (2003). Symbols are defined in Fig. 3.12.*

two molecules. The CS/SO ratio varies from $\approx$ 0.2 to 4, in good agreement with the results of Nilsson et al. (2000) who analyzed CS and SO abundances from a sample of 19 molecular clouds.

SO_2 is detected toward only a few sources in the sample. Typically, the upper limit to the SO_2 abundance is found to be a few$\times 10^{-10}$ in this study. The same was seen by Buckle & Fuller (2003) who only detected SO_2 emission toward 30% of their sources, i.p., sources in the Serpens region. In fact, Buckle & Fuller did not detect SO_2 for any of the four sources also in our sample. For these sources upper limits based on the observations of Buckle & Fuller are a few$\times 10^{-11}$.

The non-detections can also be compared to the results of Schöier et al.

(2002) for IRAS 16293-2422, for which abundance jumps, either due to thermal evaporation or outflow-induced shocks, were found. Schöier et al. argued for an SO_2 abundance jump from 2×10^{-10} in the outer envelope to 1×10^{-7} in the inner envelope. The SO_2 lines in this study are in fact expected to probe the outer region of the envelope and the derived upper limit to the abundances do seem to indicate that the abundances found for IRAS 16293-2422 are higher than those found here. It is interesting to note that SO_2 is only detected toward regions with high outflow activity (i.p., the objects in NGC 1333 and VLA1623) and that the SO 8_7-7_6 was found to be very broad (and only detected) toward these objects with widths of $\sim 5-10$ km s^{-1} (FWHM) contrasting the other observed lines. These objects also show the highest SO abundances. Together with the strong SO and SO_2 emission toward the Serpens sources which are also related to strong outflows, this suggests an enhancement of sulfur-bearing species in the inner envelopes due to outflows. Large enhancements of the sulfur-species (together with CH_3OH and SiO) are observed in outflows where these can be studied well separated from their driving protostar (Bachiller & Pérez Gutiérrez 1997; Jørgensen et al. 2004a). A deep systematic study of the line emission from these and other sulfur species (e.g., H_2S, HCS^+, H_2CS) toward a large sample of objects will shed more light on this question and thus provide better insight into the sulfur-chemistry in low-mass protostars.

3.4.3 HCO^+ and N_2H^+

HCO^+ is of great importance in chemical models of protostellar environments as it is the primary molecular ion and thus regulator of the electron density and ionization structure (e.g., Caselli et al. 2002b) and the most important destroyer of other molecules (e.g., Bergin & Langer 1997).

As shown in the upper panel of Fig. 3.14, the derived HCO^+ abundances show an evolution with mass similar to that found for CO (Chapter 2). This is even more clearly illustrated in the lower panel of Fig. 3.14, where a tight correlation between CO and HCO^+ abundances is seen. In fact, the CO and HCO^+ abundances are linearly dependent with

$$[\mathrm{HCO^+}] = 7.4 \times 10^{-5} \times [\mathrm{CO}]$$

or put differently: a "standard" undepleted CO abundance of 10^{-4} corresponds to an HCO^+ abundance of 7.4×10^{-9}.

It is found that N_2H^+ marks a clear contrast to HCO^+: as shown in Fig. 3.15 the N_2H^+ abundance decreases with increasing CO abundance. High angular resolution interferometer maps of protostellar regions (e.g., Bergin et al. 2001; Jørgensen et al. 2004b) find that cores with low CO abundances show up stronger when mapped in N_2H^+.

Both trends can be understood when considering the chemical network in more detail taking the depletion of CO into account. For both HCO^+ and N_2H^+ the primary formation routes are through reactions with H_3^+, i.e.:

$$\mathrm{H_3^+ + CO \rightarrow HCO^+ + H_2} \tag{3.6}$$

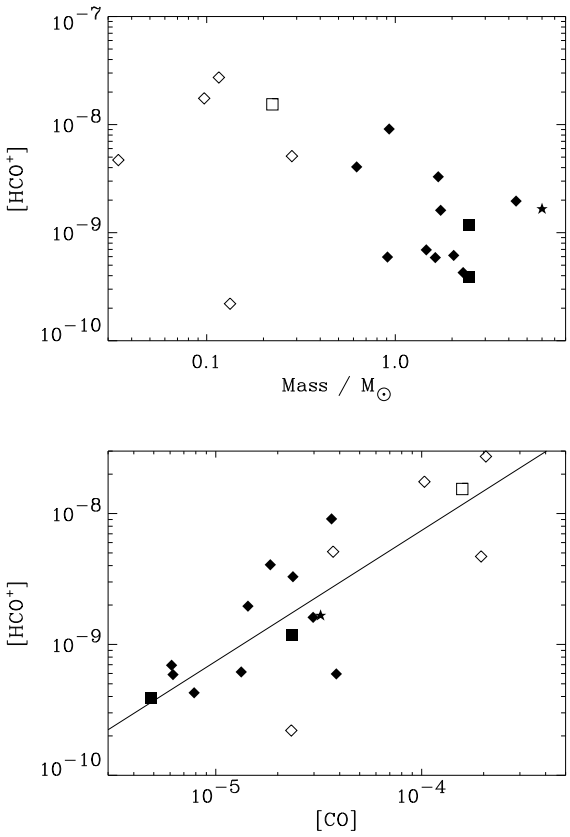

Figure 3.14. *HCO$^+$ abundance vs. mass (upper panel) and vs. CO abundance (lower panel). In the lower panel has the linear correlation between the HCO$^+$ and CO abundances been overplotted. Symbols defined as in Fig. 3.12.*

$$H_3^+ + N_2 \rightarrow N_2H^+ + H_2 \tag{3.7}$$

For standard CO abundances ([CO/H_2] $\sim 10^{-4}$) eq. (3.6) is the dominant removal mechanism for H_3^+, but as CO freezes out this reaction drops in importance and eq. (3.7) becomes more important for the removal of H_3^+. The main destruction mechanism for HCO^+ is dissociative recombination, which is also the case for N_2H^+ when CO is depleted. However, as CO returns to the gas-phase, destruction of N_2H^+ through reactions with CO:

$$N_2H^+ + CO \rightarrow HCO^+ + N_2 \tag{3.8}$$

becomes the dominant removal mechanism for N_2H^+. In Appendix 3.5 we consider the chemical network for H_3^+, HCO^+, and N_2H^+ in detail. The main

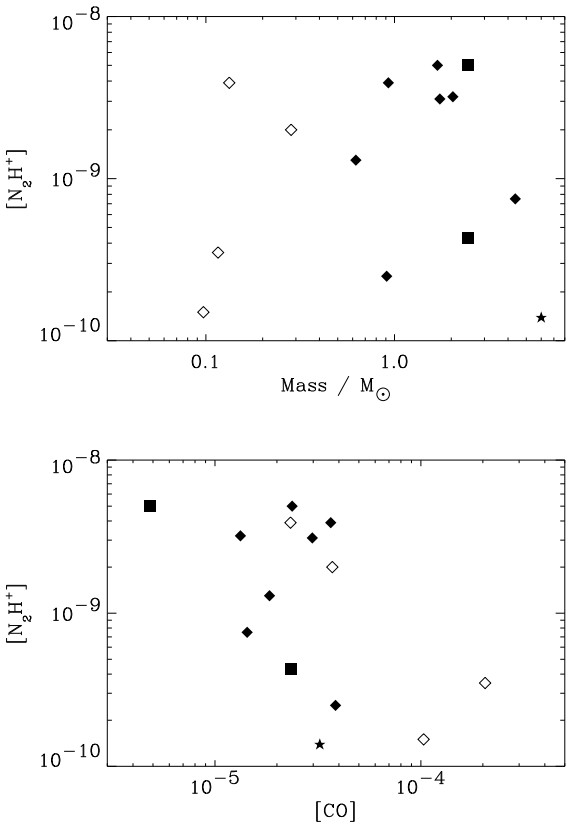

Figure 3.15. *N_2H^+ abundance vs. mass (upper panel) and vs. CO abundance (lower panel). Symbols as in Fig. 3.12.*

conclusions are that a linear increase of the HCO^+ abundance with CO abundance is expected when CO is depleted. For higher CO abundances, however, the HCO^+ abundance does not depend on [CO] since a balance between formation through eq. (3.6) and destruction through dissociative recombination exists. In contrast the N_2H^+ abundance is high when CO is depleted but declines rapidly as $([\mathrm{CO}])^{-2}$ with the increasing CO abundance as H_3^+ is removed (forming HCO^+) and N_2H^+ is destroyed through eq. (3.8).

To further illustrate these points the upper panel of Fig. 3.16 shows the chemical network for low (depleted) and standard CO abundances. The lower panel shows the N_2H^+, HCO^+ and H_3^+ abundances as functions of CO abundance calculated in a cell with density $n(\mathrm{H_2}) = 1 \times 10^6\ \mathrm{cm}^{-3}$ and temperature $T = 20$ K at 10^4 years using the chemical code of S.D. Doty and adopting the chemistry used in the detailed chemical modeling of the envelope around

IRAS 16293-2422 (Doty et al. 2004). The figure clearly shows the linear relationship between the CO and HCO^+ abundances for CO values lower than $\approx 2\times10^{-5}$ and likewise the rapid decline of N_2H^+ for higher CO abundances. The absolute values of the abundances and the exact CO abundance dividing between the "low" and "standard" [CO] regions is regulated by the exact details of the chemistry (e.g., the initial N_2 abundance) and the cosmic ray ionization rate, but the overall trends remain the same. Thus trends of a linear increase of HCO^+ abundance with increasing CO abundance can be understood in a limit where CO is depleted and Eq. (3.6) is no longer the dominant removal mechanism for H_3^+.

3.4.4 HCN, HNC and CN

HCN is the molecule with the most striking lack of correlation with mass or CO abundances, as can be seen in Fig. 3.18. Chemically HCN and its geometrical isomer, HNC, are naturally thought to be closely related and [HNC]/[HCN] ratios of unity or slightly higher are typically observed toward molecular clouds (Hirota et al. 1998; Dickens et al. 2000).

For both HCN and HNC it is found that the 1–0 lines trace material with higher abundances - or additional material outside what can be described by the single power-law density models. As seen in Fig. 3.17 the [HCN/H^{13}CN] ratio is significantly lower than 70 quoted by Wilson & Rood (1994). One exception is the case of N1333-I4B which has a high estimated HCN abundance, possibly related to confusion with the outflow. This ratio is, however, not correlated with mass, as would be expected in case of an error in the opacity treatment of the lines. The explanation is more likely that the H^{13}CN abundances are heavily biased toward determinations based on the low J lines observed with the Onsala telescope since the higher J lines are only detected toward a small fraction of the sources. Since the abundances derived on the basis of the isotopic H^{13}CN thereby probe the outermost, less depleted regions this should lower the estimated [HCN/H^{13}CN] ratios.

A higher degree of CO depletion could be expected to lead to a removal of gas-phase carbon and oxygen and thereby a decline of the [HNC]/[HCN] and [CN]/[HCN] ratios. On the other hand it is found that neither the [CN]/[HCN] nor the [HNC]/[HCN] ratio correlate with the degree of CO depletion. Another option is destruction of HNC at higher temperatures through neutral-neutral reactions. This would be in agreement with the result that the Orion molecular clouds have significantly lower HNC abundances relative to HCN (Schilke et al. 1992) than the dark clouds surveyed by Hirota et al. (1998).

Fig. 3.19 illustrates the close correlation between the HNC and CN abundances also indicated by the correlation coefficients (Table 3.16 and Fig. 3.11). HNC and CN are expected to be related, with $HCNH^+$ as an intermediate product, through the reactions:

$$\mathrm{HNC} + \mathrm{H_3^+} \rightarrow \mathrm{HCNH^+} + \mathrm{H_2} \tag{3.9}$$

$$\mathrm{HCNH^+} + \mathrm{e^-} \rightarrow \mathrm{CN} + \mathrm{H_2} \tag{3.10}$$

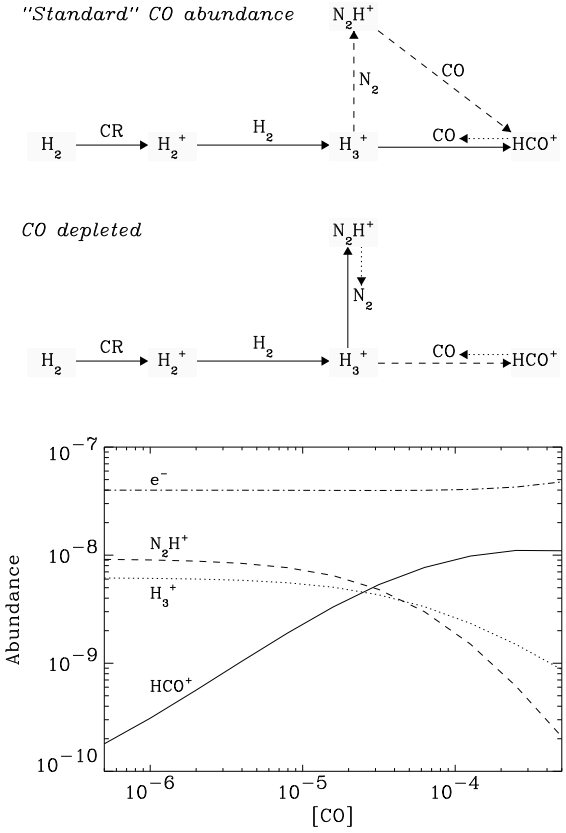

Figure 3.16. *Upper panel: the chemical networks for low CO abundances (i.e., depletion) and standard CO abundance ([CO]*$\sim 10^{-4}$*). The dominant reactions are indicated by solid arrows, secondary reactions by dashed arrows. Where dissociative recombination is the main destruction for a molecule (i.e.,* N_2H^+ *or* HCO^+*) this has been indicated by a dotted arrow. Lower panel: the electron,* N_2H^+*,* H_3^+*, and* HCO^+ *abundances as functions of CO abundance in a cell with density* $n(\mathrm{H_2}) = 1{\times}10^6\ \mathrm{cm}^{-3}$ *and temperature* $T = 20$ *K.*

These reactions are according to the UMIST database (Le Teuff et al. 2000) the dominant formation and removal mechanisms for the three species at 20 K and $1{\times}10^6$ cm^{-3}. The main formation mehcanism for HCN at this temperature and density is also through dissociative recombination for $HCNH^+$ but this is secondary compared to the formation of CN, which could explain the weaker correlation between HCN and the other nitrogen-bearing species.

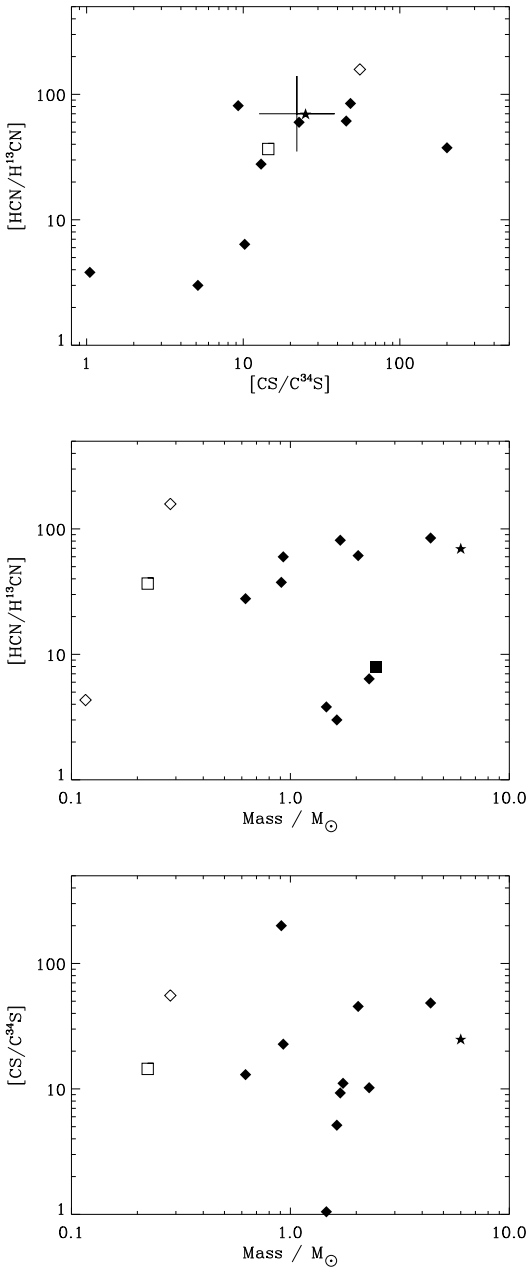

Figure 3.17. *The ratio of the CS and $C^{34}S$ abundances plotted vs. HCN and $H^{13}CN$ ratio. The big cross mark the predictions from the standard isotopic ratio of ^{12}C:^{13}C of 70 and ^{32}S:^{34}S of 22. Symbols as in Fig. 3.12.*

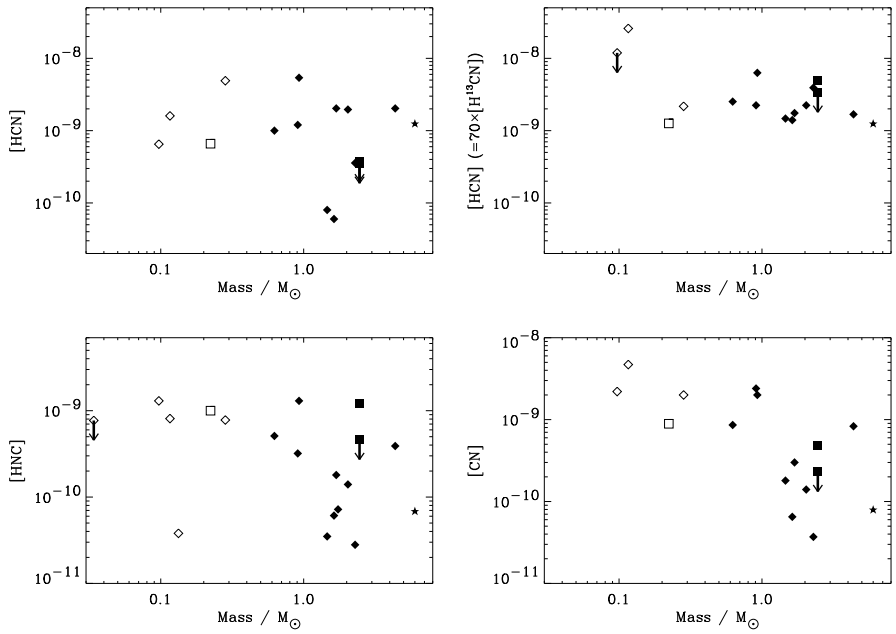

Figure 3.18. *HCN abundances derived on the basis of main isotopic species and $H^{13}CN$ (upper panels, left and right) and CN and HNC abundances (lower panels) vs. mass. As in previous figures, the class 0 objects are indicated by "♦", the class I objects by "◊" and the pre-stellar cores by "■" with the class 0 objects VLA1623 and IRAS 16293-2422 singled out by "□" and "★", respectively.*

3.4.5 HC_3N

The HC_3N abundance has been suggested to be an indicator of the temporal evolution or the degree of depletion (e.g., Hirahara et al. 1992; Ruffle et al. 1997; Caselli et al. 1998) in dark clouds and pre-stellar cores. The HC_3N abundance peaks early in the evolution of dark clouds when a substantial amount of carbon is in atomic form in the gas-phase, but also increases with increasing depletion (i.e., potentially at "later" stages). Depletion tends to remove atomic oxygen from the gas-phase, which otherwise has a tendency to destroy ions necessary for the formation of species such as HC_3N. Fig. 3.20 compares the HC_3N abundance with the CO abundance and the CS/SO abundance ratio. As can be seen, [HC_3N] is not particularly higher in objects with a larger degree of CO depletion - except for the pre-stellar cores when these are considered separately (see Sect. 3.4.7).

For the protostars in our sample, however, Fig. 3.20 shows that the HC_3N abundance is related to the [CS]/[SO] ratio - with lower ratios of the two sulfur-bearing molecules corresponding to lower HC_3N abundances. This can be understood in a scenario where the HC_3N abundance is indeed a tracer of atomic

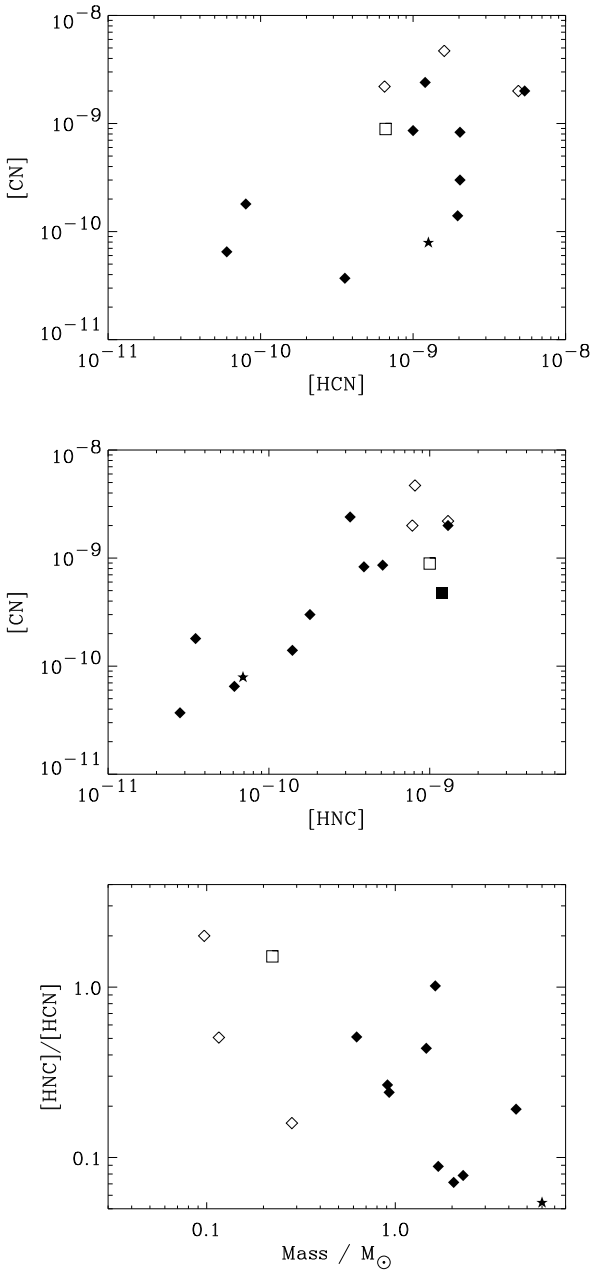

Figure 3.19. *[CN] vs. [HCN] (upper panel) and vs. [HNC] (lower panel). Symbols as in Fig. 3.12.*

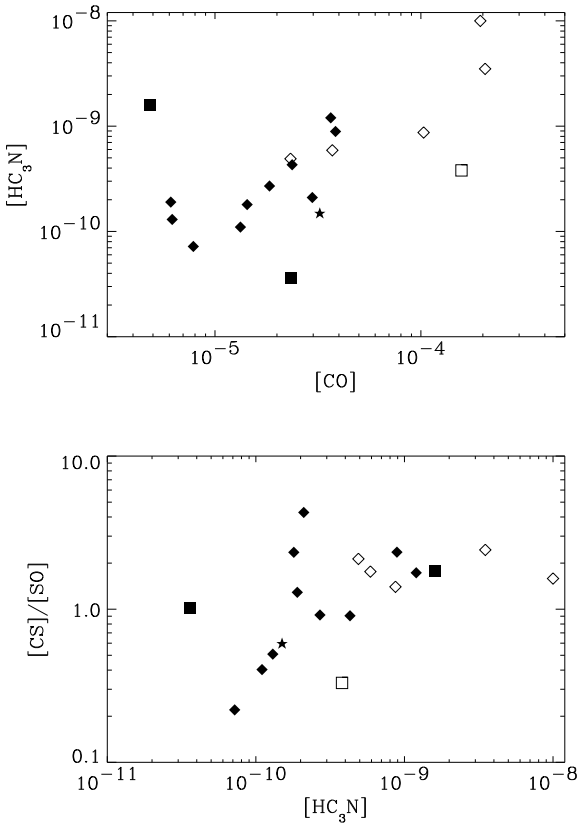

Figure 3.20. *[HC_3N] vs. mass and [CO] (upper panel) and vs. [CS]/[SO] ratio (lower panel). Symbols as in Fig. 3.12.*

carbon, since the CS/SO ratio would likewise be increased by higher amounts of atomic carbon, as suggested by the models of Bergin et al. (1997). The question is then whether this should be taken as an indicator of chemical "youth". As can be seen in Fig. 3.20, the dynamically "older" class I objects have higher HC_3N abundances and [CS]/[SO] ratios, which apparently would contradict this suggestion.

An alternative explanation could be that the amount of atomic carbon is enhanced by the impact of UV radiation from the outside due to the interstellar radiation field. We can, however, argue that this is not the case from the CN line observations. As noted above the HC_3N and CN abundances are found to be interlinked, which is not difficult to understand if one considers the dominant formation and destruction mechanisms for HC_3N in gas where the degree of

CO depletion is low:

$$\mathrm{CN} + \mathrm{C_2H_2} \rightarrow \mathrm{HC_3N} + \mathrm{H}$$

$$\mathrm{C^+} + \mathrm{HC_3N} \rightarrow \mathrm{C_3H^+} + \mathrm{CN}$$

If the trend seen between the HC_3N and the CS/SO ratio is related to the radiation field, the correlation should be more clear for abundances constrained by the CN 1–0 lines which probe the outermost region of the envelope. As illustrated in Fig. 3.21, however, the trend is much stronger for the CN abundances constrained by the CN 3–2 lines that have a significantly higher critical density and thus probe the inner, more shielded region of the envelope. UV radiation from the central star could increase the amount of atomic carbon in the inner envelope and would lead to trends similar to that observed, but whether UV radiation can penetrate far enough out into the envelope to be important is still not clear. A more detailed study of the molecular species in the chemical network for the nitrogen-bearing species together with more detailed modeling including the radial variation of the molecular abundances is needed to fully address these questions.

3.4.6 Deuterium fractionation

The deuterium fractionation of HCO^+ is seen from plots of the $[DCO^+]/[HCO^+]$ ratio in Fig. 3.22. The fact that the DCO^+ emission predominantly originates in the cold outer gas is evidenced by the narrow line widths for all sources: the turbulent broadening required to model the DCO^+ line widths is only 0.3-0.5 km s^{-1}. The prestellar cores clearly show the highest $[DCO^+]/[HCO^+]$ ratio of $\sim$5% in agreement with findings by, e.g., Caselli et al. (2002b). The class 0 sources show $[DCO^+]/[HCO^+]$ ratios ranging from 0.004 to 0.05. DCO^+ is not detected for the class I sources corresponding to the upper limits on the $[DCO^+]/[HCO^+]$ ratio of ~ 0.001. As can be seen from the lower panel of Fig. 3.22, the $[DCO^+]/[HCO^+]$ ratio does seem to be correlated with the degree of CO depletion.

The typical deuterium abundance ratios are in general significantly higher than the "cosmic" D/H ratio of 10^{-5}. Both gas-phase reactions and grain-surface reactions have been invoked to describe the deuterium fractionation at low temperatures in pre- and protostellar environments. In gas-phase models by Roberts & Millar (2000b) such a trend is indeed expected. In pure gas-phase models the primary mechanism for driving the fractionation of HCO^+ is the small zero-point energy in the reaction:

$$\mathrm{H_3^+} + \mathrm{HD} \leftrightarrows \mathrm{H_2D^+} + \mathrm{H_2} \tag{3.11}$$

that predominantly drives the D into H_2D^+ relative to H_3^+, and which subsequently reacts with CO to form DCO^+. Depletion of CO causes (3.11) to be the dominant mechanism for removal of H_3^+ and since DCO^+ is produced subsequently, the formation of HCO^+ (eq. (3.6) in Sect. 3.4.3) will be less productive compared to the deuterated versions. Models by Roberts & Millar (2000a) and

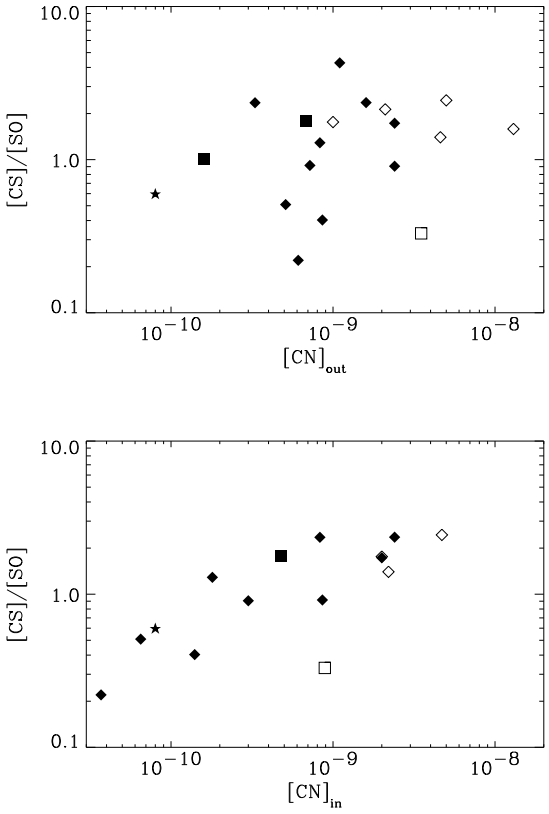

Figure 3.21. *CS/SO abundance ratio vs. abundance of CN constrained by the 1–0 lines (upper) and 3–2 lines (lower) probing the outer and inner regions of the envelope, respectively. Symbols as in Fig. 3.12.*

Roberts et al. (2003) show that a high degree of depletion may be required in order to produce formation of the doubly and triply deuterated species observed in protostellar environments (Ceccarelli et al. 1998; Lis et al. 2002; Parise et al. 2002; van der Tak et al. 2002). Other studies indicate an increase of the deuteration with CO depletion, e.g., the survey of the deuteration of D_2CO for a sample of pre-stellar cores by Bacmann et al. (2003).

Figure 3.23 compares the [DCN]/[HCN] ratio with envelope mass and the $[DCO^+]/[HCO^+]$ ratio. No correlation is seen between the [DCN]/[HCN] and $[DCO^+]/[HCO^+]$ ratios. In fact the absence of DCN in the pre-stellar cores is striking considering their strong DCO^+ emission. This could imply that the [DCN]/[HCN] ratio is higher for the warmer envelopes. This is in agreement with gas-phase deuteration of HCN, which may occur at slightly higher tem-

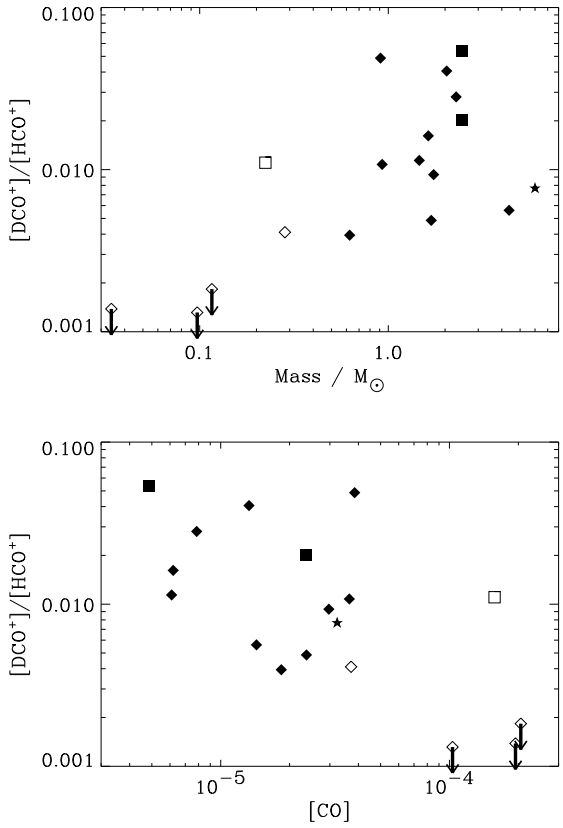

Figure 3.22. *[DCO$^+$]/[HCO$^+$] ratio vs. mass (upper panel) vs. and [CO] (lower panel). Symbols as in Fig. 3.12.*

peratures than that of HCO$^+$: in particular deuteration through $CH_3^+ + HD \rightarrow CH_2D^+$ may be more important for temperatures higher than $\approx$ 30 K (e.g., Turner 2001). Alternatively, the [DCN]/[HCN] ratio may have been established earlier in the protostellar evolution, frozen out onto the dust grains and released back at higher temperatures than is the case for the [DCO$^+$]/[HCO$^+$] ratio.

3.4.7 The pre-stellar cores

The two pre-stellar cores in our sample, L1689B and L1544, were also studied by Lee et al. (2003) together with an additional core, L1512. Lee et al. found a high degree of depletion of CO and HCO$^+$ for L1544 but close to "standard" abundances for these molecules in L1689B. This is consistent with the results in

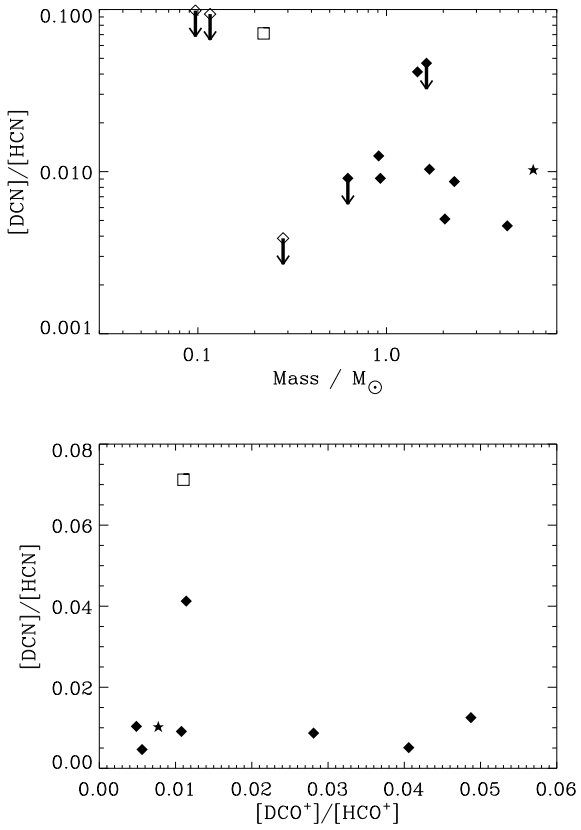

Figure 3.23. *[DCN]/[HCN] abundance vs. mass (upper panel) and [DCO^+]/[HCO^+] ratio (lower panel). Symbols as in Fig. 3.12.*

this paper. Lee et al. also observed N_2H^+ 1–0 and found it to be weak in L1689B compared to L1544. This is in good agreement with our results which show N_2H^+ to be an order of magnitude more abundant in L1544 than in L1689B, strengthening the N_2H^+ and CO anti-correlation discussed in Sect. 3.4.3. Of the other molecules in this paper, the sulfur-bearing species (CS and SO) are also found to have lower abundances in L1544 indicating a higher degree of overall depletion. The nitrogen-bearing species in contrast show an opposite trend with high abundances in L1544. In particular, HC_3N is close to a factor of 50 higher in L1544 than in L1689B, supporting the suggestion that HC_3N traces the degree of depletion in the pre-stellar stages (e.g. Ruffle et al. 1997; Caselli et al. 1998). Also the higher degree of HCO^+ deuteration in L1544 than in L1689B is consistent with the higher degree of depletion L1544 than in L1689B (ref. the discussion in Sect. 3.4.6).

3.4.8 Comparison to other star-forming regions

In Fig. 3.10 the average abundances for the class 0 and I objects and pre-stellar cores are compared to the abundances of other star-forming regions, the outer envelope around the class 0 object IRAS 16293-2422 (Schöier et al. 2002), the average abundance for the 3 high-mass YSOs W3(IRS4), W3(IRS5) and W3(H2O) (Helmich & van Dishoeck 1997) and the "C" position of the dark cloud L134N (Dickens et al. 2000).

As mentioned in the introduction the class 0 object IRAS 16293-2422 is the most studied low-mass protostar in terms of the chemistry of its protostellar envelope (see, e.g., Blake et al. 1994; van Dishoeck et al. 1995; Ceccarelli et al. 1998, 2000a,b; Schöier et al. 2002; Parise et al. 2002; Cazaux et al. 2003), because of its rich spectrum and its warm inner region where ices have evaporated. This naturally raises the question whether IRAS 16293-2422 is indeed a typical class 0 object: is the richness of its spectrum simply caused by it being the closest object with the most massive envelope, or is it caused by other effects, such as the interaction of its outflow with the nearby envelope? As it can be seen from Table 3.15 and Fig. 3.12-3.23 IRAS 16293-2422 has a fairly standard set of outer envelope abundances for CO, CS and HCN. On the other hand it shows lower abundances (factors 4-20) of especially HNC, CN and N_2H^+ and high abundances of SO and SO_2 compared to the typically upper limit found for the objects in this study. It does not, however, stand markedly out considering the scatter in abundances within the larger group of class 0 objects. It therefore seems that IRAS 16293-2422, despite possibly being affected by outflows on smaller scales (e.g., Schöier et al. 2004a) and having a "hot inner region" (e.g., Ceccarelli et al. 1998; Schöier et al. 2002) has a cold outer envelope that is similar to that of the other class 0 objects in terms of the overall abundances. Otherwise the most striking feature of Fig. 3.10 is the significantly higher HNC abundance (two orders of magnitude) in L134N compared to the other sources and molecules. The high- and the low-mass YSOs differ slightly with SO and HCN abundances higher by up to a factor 5 and HC_3N lower by a factor 5-10 in the high-mass YSOs.

3.5 Conclusion

The molecular inventories for the envelopes around a sample of low-mass protostars have been established. Using models for the one dimensional physical structure of the envelopes from Jørgensen et al. (2002) (Paper I), the abundances of a range of molecular species are constrained through Monte Carlo line radiative transfer modeling of single-dish submillimeter and millimeter observations. The main conclusions are:

1. For most sources and molecules, the high excitation 0.6-1.4 mm lines are well represented by a constant fractional abundance. The low excitation 3 mm lines of HCO^+ and the nitrogen-bearing species, however, are signifcantly underestimated by such models, similar to the trend seen for

CO in Paper I. Varying freeze-out timescales in the regions of the envelopes corresponding to different densities can explain this. All lines for these species can be accounted for with a "drop" profile where the envelopes have "standard" molecular abundances in the outermost low density region and in the innermost high temperature region, but drops in an intermediate zone where the molecule can freeze-out.

2. Effects of the envelope velocity field are tested and confirmed to be insignificant when determining the abundances from optically thin species. An upper limit to the magnitude of the velocity field and thereby the mass accretion rate can be inferred from comparison to the widths of those lines.

3. An empirical chemical network is constructed through calculations of correlation coefficients for pairs of abundances. Strong correlations are found between, e.g., HCO^+ and CO, CS and SO and between the nitrogen-bearing species, HNC, CN and HC_3N.

4. A linear relationship between the abundances of CO and HCO^+ is seen, whereas the N_2H^+ abundances appear lower in the objects with high CO abundances. This can be understood from analytic considerations of the chemical network of HCO^+ and N_2H^+, where both are formed through reactions involving H_3^+. A linear relationship between [CO] and [HCO^+] exist in the limit where N_2 rather than CO removes H_3^+ due to CO freeze-out. Likewise the N_2H^+ abundances rapidly decline as soon as the CO abundances increase, because H_3^+ and N_2H^+ are destroyed through reactions with CO.

5. The CS/SO abundance ratio is found to be correlated with the abundances of CN and HC_3N, which may reflect the amount of atomic carbon in the gas-phase.

6. High levels of deuterium fractionation of HCO^+ ([DCO^+]/[HCO^+] = 1-5 %) are found in the pre-stellar cores and in the most massive/coldest envelopes around the class 0 objects. The [DCN]/[HCN] ratio is not correlated with the [DCO^+]/[HCO^+] ratio, possibly indicating differences in the gas-phase deuteration of HCO^+ and HCN.

7. Among the two pre-stellar cores in our sample, L1544 shows a higher degree of depletion of CO and the sulfur-bearing species, resulting in a chemistry with higher abundances of N_2H^+, HC_3N and a higher degree of HCO^+ deuteration than what is seen in L1689B.

8. The outer abundances of the previously studied class 0 object IRAS 16293-2422 (e.g., Schöier et al. 2002) are found to be in agreement with the average abundances in the studied sample of class 0 objects, indicating that the chemistry of the outer cold envelope of this particular object is similar to that of other class 0 objects.

The results of this paper show the potential of multi-transition line observations to understand radial variations and find empirical correlations between various species elucidating the chemistry in star-forming environments. Future observational studies should focus on deeper systematic searches, e.g., in order to fully understand the sulfur chemistry and to constrain abundances of species connecting the nitrogen-bearing species to the overall chemical network. Also high-resolution observations with, e.g., the SMA, CARMA and ALMA can be used to test the predictions of radial variations; as discussed elsewhere (Jørgensen et al. 2004b; Schöier et al. 2004a) the models presented here serve as a valuable starting point for interpreting such data. This study has not addressed the chemistry of the innermost hot core region where complex organic molecules may be formed through evaporation of ices and high-temperature gas-phase chemistry. Since these regions are small (typically < 1" for the objects considered here), high angular resolution observations of high-excitation lines are needed to probe them. Finally, the results presented here will form the basis for more detailed modeling of the envelope chemistry.

Acknowledgements

This work is the result of an extensive observing program at the James Clerk Maxwell Telescope (JCMT) on Hawaii. The authors are grateful to the JCMT staff, in particular Remo Tilanus, for excellent technical assistance and support before, during and after numerous observing sessions. Thanks also goes to various observers who have carried out parts of the observations in "service" mode. We are especially grateful to Sebastien Maret and Cecilia Ceccarelli for useful discussions and for the IRAM 30 m observations. Michiel Hogerheijde and Floris van der Tak are acknowledged for making their Monte Carlo code publically available and for helpful discussions. We are also grateful to Steve Doty for the use of his chemical code. Participation in conferences, where parts of these results were presented and discussed, were financially supported by Leids Kerkhoven-Bosscha Fond. The work of JKJ is funded by the Netherlands Research School for Astronomy (NOVA) through a Ph.D. stipend and research in astrochemistry in Leiden is supported by a NWO Spinoza grant. FLS further acknowledges support from the Swedish Research Council.

Appendix: The chemical network for HCO^+, N_2H^+, and H_3^+

This appendix explores the chemical network for HCO^+, N_2H^+, and H_3^+ (see Fig. 3.16). As discussed in Sect. 3.4.3 the dominant formation and destruction mechanisms for HCO^+ are:

$$H_3^+ + CO \rightarrow HCO^+ + H_2 \tag{3.12}$$

$$HCO^+ + e^- \rightarrow CO + H \tag{3.13}$$

The main formation mechanism for N_2H^+ is:

$$H_3^+ + N_2 \rightarrow N_2H^+ + H_2 \tag{3.14}$$

When the CO abundance is low the main removal mechanism for N_2H^+ is through dissociative recombination:

$$N_2H^+ + e^- \rightarrow N_2 + H \tag{3.15}$$

whereas for "standard" CO abundances of 1×10^{-4} the main removal mechanism becomes:

$$N_2H^+ + CO \rightarrow N_2 + HCO^+ \tag{3.16}$$

For H_3^+ the main formation route is through cosmic ray ionization of H_2:

$$H_2 + CR \rightarrow H_2^+ + e^-$$

$$H_2^+ + H_2 \rightarrow H_3^+ + H \tag{3.17}$$

The main removal mechanism for H_3^+ is through eq. (3.14) when the CO abundance is low and through eq. (3.12) when the CO abundance is close to the standard value $\sim 10^4$.

We introduce the rate coefficients for each reaction with k_{HCO^+}, k_{CO}, and $k_{N_2H^+}$ being the rate coefficients for eq. (3.12), (3.13), and (3.14), respectively, and k_{N_2} and k'_{N_2} being the rate coefficients for eq. (3.15) and (3.16), respectively.

We can equate the formation and destruction rates of HCO^+ as:

$$k_{HCO^+}\, n_{H_3^+}\, n_{CO} \;=\; k_{CO}\, n_{HCO^+}\, n_e \tag{3.18}$$

where n_{HCO^+}, $n_{H_3^+}$, n_{CO} and n_e are the densities of HCO^+, H_3^+, CO and electrons, respectively.

When the CO abundance is $\sim 10^{-4}$ the main removal mechanism for H_3^+ is eq. (3.12), so equating the formation and destruction rate for H_3^+ gives:

$$\zeta\, n_{H_2} \;=\; k_{HCO^+}\, n_{H_3^+}\, n_{CO} \tag{3.19}$$

where ζ is the cosmic ray ionization rate, n_{H_2} the H_2 density and it is assumed that each H_2^+ molecular ion produced in eq. (3.17) immediately reacts with H_2 to form H_3^+. From eq. (3.18) and (3.19) we can then write:

$$\zeta\, n_{H_2} \;=\; k_{CO}\, n_{HCO^+}\, n_e \tag{3.20}$$

which dividing by $n_{H_2}^2$, introducing the abundances $[X] = n_X/n_{H_2}$ and isolating $[HCO^+]$ gives:

$$[HCO^+] = \frac{\zeta/n_{H_2}}{k_{CO}\,[e]} \tag{3.21}$$

We can similarly equate the formation and destruction rates for N_2H^+ (eq. (3.14) and (3.16)):

$$k_{N_2H^+}\, n_{H_3^+}\, n_{N_2} \;=\; k'_{N_2}\, n_{N_2H^+}\, n_{CO} \tag{3.22}$$

which together with eq. (3.19) gives (eliminating $n_{H_3^+}$):

$$k_{N_2H^+}\, n_{N_2}\, \frac{\zeta\, n_{H_2}}{k_{HCO^+}\, n_{CO}} = k'_{N_2}\, n_{N_2H^+}\, n_{CO} \tag{3.23}$$

which can be rewritten in terms of the N_2H^+ abundance:

$$[N_2H^+] = \frac{[N_2]}{[CO]^2} \frac{k_{N_2H^+}}{k'_{N_2}\, k_{HCO^+}} \zeta / n_{H_2} \tag{3.24}$$

In the low [CO] limit the main removal mechanism for H_3^+ is by eq. (3.14) rather than by eq. (3.12), so in this limit we write for the formation/destruction balance for H_3^+

$$\zeta n_{H_2} \;=\; k_{N_2H^+}\, n_{H_3^+}\, n_{N_2} \tag{3.25}$$

replacing eq. (3.19). From eq. (3.18) and (3.25) we can then eliminate n_{HCO^+}:

$$n_{HCO^+} = n_{CO} \frac{k_{HCO^+}}{k_{CO}} \frac{\zeta\, n_{H_2}}{n_e\, k_{N_2H^+}\, n_{N_2}} \tag{3.26}$$

or in terms of the abundances:

$$[HCO^+] = \frac{k_{HCO^+}}{k_{CO}\, k_{N_2H^+}} \frac{\zeta / n_{H_2}}{[e]\,[N_2]} [CO] \tag{3.27}$$

Furthermore, in this limit the destruction of N_2H^+ is by dissociative recombination (eq. (3.15), so for N_2H^+ we can write:

$$k_{N_2H^+}\, n_{H_3^+}\, n_{N_2} \;=\; k_{N_2}\, n_e\, n_{N_2H^+} \tag{3.28}$$

and again eliminating $n_{H_3^+}$, rewriting the expression in terms of abundances, we find:

$$[N_2H^+] = \frac{\zeta / n_{H_2}}{k_{N_2}\,[e]} \tag{3.29}$$

The main points to be drawn from these equations (i.p., eq. (3.21), (3.24), (3.27) and (3.29)) are that the HCO^+ abundance does not depend on the CO abundance in the "high" [CO] limit, whereas the N_2H^+ abundance declines quickly as $([CO])^{-2}$. In the low [CO] limit, however, the HCO^+ abundance increases linearly with increasing CO abundance whereas the N_2H^+ abundance is constant.